LAWRENCE
LIVERMORE
NATIONAL
LABORATORY

UCRL-JRNL-222113

An Arbitrary Lagrangian-Eulerian Discretization of MHD on 3D Unstructured Grids

R. N. Rieben, D. A. White, B. K. Wallin, J. M. Solberg

June 15, 2006

Journal of Computational Physics

Updated October 14, 2003

An Arbitrary Lagrangian-Eulerian Discretization of MHD on 3D Unstructured Grids

R. N. Rieben [a,*], D. A. White [a], B. K. Wallin [b], J. M. Solberg [c]

[a] *Defense Sciences Engineering Division, Lawrence Livermore National Laboratory*

[b] *Scientific B-Division, Lawrence Livermore National Laboratory*

[c] *Defense Technologies Engineering Division, Lawrence Livermore National Laboratory*

Abstract

We present an arbitrary Lagrangian-Eulerian (ALE) discretization of the equations of resistive magnetohydrodynamics (MHD) on unstructured hexahedral grids. The method is formulated using an operator-split approach with three distinct phases: *electromagnetic diffusion, Lagrangian motion*, and *Eulerian advection*. The resistive magnetic dynamo equation is discretized using a compatible mixed finite element method with a 2nd order accurate implicit time differencing scheme which preserves the divergence-free nature of the magnetic field. At each discrete time step, electromagnetic force and heat terms are calculated and coupled to the hydrodynamic equations to compute the Lagrangian motion of the conducting materials. By virtue of the compatible discretization method used, the invariants of Lagrangian MHD motion are preserved in a discrete sense. When the Lagrangian motion of the mesh causes significant distortion, that distortion is corrected with a relaxation of the mesh, followed by a 2nd order monotonic remap of the electromagnetic state variables. The remap is equivalent to Eulerian advection of the magnetic flux density with a fictitious mesh relaxation velocity. The magnetic advection is performed using a novel variant of constrained transport (CT) that is valid for unstructured hexahedral grids with arbitrary mesh velocities. The advection method maintains the divergence free nature of the magnetic field and is second order accurate in regions where the solution is sufficiently smooth. For regions in which the magnetic field is discontinuous (e.g. MHD shocks) the method is limited using a novel variant of algebraic flux correction (AFC) which is local extremum diminishing (LED) and divergence preserving. Finally, we verify each stage of the discretization via a set of numerical experiments.

Key words: Magnetohydrodynamics, Resistive MHD, Electromagnetic diffusion, Mixed finite element methods, $H(Curl)$ and $H(Div)$ - conforming methods, Discrete differential forms, Vector finite elements, Operator-splitting, Electromagnetic advection, Constrained transport, TVD schemes, Algebraic flux-correction, Unstructured grids

1 Introduction

We are interested in the simulation of magnetohydrodynamic events and electromechanical devices in three dimensions. Our primary goal is a numerical method that solves, in a self-consistent manner, the equations of electromagnetics (primarily statics and diffusion), heat transfer (primarily conduction), and non-linear mechanics (motion, elastic-plastic deformation, and mechanical contact). Example applications for these simulations include magnetic flux compression generators, metal forming, and electromagnetic launchers. In this paper, we focus on the numerical discretization of electromagnetic diffusion in an arbitrary Lagrangian-Eulerian (ALE) fashion [1] for the purposes of computing $\vec{J} \times \vec{B}$ forces and $\vec{J} \cdot \vec{E}$ resistive energy losses for coupling to hydrodynamic and thermal calculations in an operator split fashion. All computational results were obtained by incorporating ALE electromagnetics into a well-known ALE hydrodynamic code, ALE3D, which has been successfully used in a wide variety of computational physics applications including [2], [3],[4], [5], [6],[7], and [8]. In this paper, the discretization of the hydrodynamics is not discussed in detail.

In multiphysics ALE hydrodynamic codes, an operator split method is typically employed where separate physics packages are run sequentially and update their variables in the Lagrangian frame. When the Lagrange motion of the mesh causes significant mesh distortion, that distortion is corrected with an equipotential relaxation of the mesh, followed by a 2nd order monotonic remap of field quantities. This remap is equivalent to advection of field quantities through the mesh with a fictitious effective velocity determined by the amount of mesh relaxation. In our proposed ALE formulation of MHD, we will employ an operator-split method with three distinct steps:

- *Electromagnetic Diffusion* – Solve the equations of electromagnetic diffusion in the Lagrangian frame at one discrete time step for fixed materials.
- *Lagrangian Motion* – Move mesh nodes according to $\vec{J} \times \vec{B}$ forces assuming a $\frac{d\vec{B}}{dt} = 0$ "frozen in flux" condition.
- *Eulerian Advection* – Only required if mesh is relaxed, advect (or transport) magnetic state variables to new mesh while preserving the divergence-free nature of the magnetic flux density.

While much progress has been made in obtaining numerical algorithms for coupled advection / diffusion of magnetic fields [9], [10], there are several key obstacles to be overcome for a fully three dimensional ALE finite element implementation on

* Corresponding author.
Email address: rieben1@llnl.gov (R. N. Rieben).

[1] This work was performed under the auspices of the U.S. Department of Energy by the University of California, Lawrence Livermore National Laboratory under contract No. W-7405-Eng-48, UCRL-JRNL-XXXXXX

general unstructured hexahedral grids. One issue is the need to numerically preserve the divergence-free constraint of the magnetic flux density, $\vec{B}$ [11]. Failure to reproduce this fundamental physical property in any numerical discretization can lead to the nonphysical acceleration of conducting materials due to the presence of fictitious magnetic charge. Methods for maintaining a divergence-free velocity field for incompressible flow, such as Lagrange multiplier constraints, penalty methods, elliptic projection (divergence cleaning), and relaxation-based elliptic projection (divergence damping), can in principle be applied to magnetic fields. However, more efficient and elegant approaches are based on the fact that $\vec{\nabla} \cdot \vec{B} = 0$ is not arbitrary, but is in fact a consequence of Ampere's law. If Ampere's law is discretized in a particular manner, then $\vec{\nabla} \cdot \vec{B} = 0$ is satisfied exactly without any additional effort, and this is the basis of constrained transport methods [12], [13]. Our proposed algebraic constrained transport discussed in Section 5.1 is a generalization of constrained transport for unstructured ALE simulations.

For our applications, an additional issue is the need to reproduce MHD shock fronts without introducing spurious oscillations in the magnetic field. Various flux limiters have been advocated for fluid dynamics, with the goal of limiting non-physical oscillations without introducing excessive artificial diffusion. These flux limiters can in principle be applied to magnetic fields, but care must be taken to not destroy the above mentioned divergence constraints. Some proposed methods and comparisons of various approaches can be found in [14], [15], [16], [17], [13], [18], [19], [20]. Our proposed algebraic flux correction discussed in Section 5.4 limits an intermediate edge-based voltage in a manner that enforces a local extremum diminishing property on the magnetic flux. This algebraic flux correction is an intermediate step in the algebraic constrained transport algorithm and hence $\vec{\nabla} \cdot \vec{B} = 0$ is still satisfied exactly.

In this paper we review magnetic diffusion in the Lagrangian frame of a deforming region, and we argue that a mixed finite element method employing $H(Curl)$ and $H(Div)$ basis functions [21] is ideally suited for discretization of this partial differential equation. The algebraic constrained transport method and algebraic flux limiter are built upon the same topological curl operator that is used in the discrete diffusion equation. Computational experiments are performed to confirm the second order convergence of the method for smooth fields, and to quantify the ability to conserve energy and preserve discontinuities for strongly shocked problems.

2 Electromagnetic Diffusion

The first step in our three part ALE formulation is to solve the equations of electromagnetic diffusion. We begin with a discussion of the relevant equations without material motion, then we discuss electromagnetic diffusion in moving materials. We assume a charge-free three dimensional domain Ω with a surface boundary Γ

and an outwardly directed surface normal direction $\hat{n}$. The domain Ω consists of a set of materials, each specified by the values of their material properties which define their equation of state.

Here we write Maxwell's equations in terms of $\vec{E}$ and $\vec{B}$,

$$\varepsilon \frac{\partial \vec{E}}{\partial t} = \vec{\nabla} \times \frac{1}{\mu} \vec{B} - \sigma \vec{E} - \vec{J}_s \tag{1}$$

$$\frac{\partial \vec{B}}{\partial t} = -\vec{\nabla} \times \vec{E} \tag{2}$$

$$\vec{\nabla} \cdot \varepsilon \vec{E} = 0 \tag{3}$$

$$\vec{\nabla} \cdot \vec{B} = 0 \tag{4}$$

with the constitutive relations

$$\vec{D} = \varepsilon \vec{E}, \;\; \vec{B} = \mu \vec{H} \tag{5}$$

For our purposes, the magnetic permeability μ, the electric permittivity ε, and the electric conductivity σ are free to be tensor valued functions of time and position. The term $\vec{J}_s$ is an independent current source included for generality and may not exist for all problems.

Consider solving Maxwell's equations within a good conductor, the following condition holds

$$\varepsilon \frac{\partial \vec{E}}{\partial t} \ll \sigma \vec{E} \tag{6}$$

and under this condition it is reasonable to neglect the displacement current term altogether. Neglecting displacement current results in diffusion rather than electromagnetic waves, and hence the numerical discretization is no longer required to resolve electromagnetic waves. Many problems of interest involve a combination of good conductors and air/vacuum regions, and clearly (6) is not valid in air. However, for our specific applications electromagnetic waves in the air are not important, and the displacement current term is still neglected, resulting in quasi-static magnetic fields in the air.

Both the electric field intensity $\vec{E}$ and the magnetic flux density $\vec{B}$ can be expressed in terms of potentials

$$\vec{E} = -\vec{\nabla}\phi - \frac{\partial \vec{A}}{\partial t} \tag{7}$$

$$\vec{B} = \vec{\nabla} \times \vec{A} \tag{8}$$

where ϕ is a scalar potential and $\vec{A}$ is a vector potential. Note that in (7), we see a specific decomposition of the total electric field

$$\vec{E} = \vec{E}^{irr} + \vec{E}^{ind} \tag{9}$$

where $\vec{E}^{irr} = -\vec{\nabla}\phi$ is the irrotational component of $\vec{E}$ and $\vec{E}^{ind} = -\frac{\partial \vec{A}}{\partial t}$ is the induced eddy current component of $\vec{E}$ due to a time varying magnetic vector potential.

Using the potentials from (7) and (8), we can rewrite Ampere's law (1) as

$$\vec{\nabla} \times \frac{1}{\mu}\vec{\nabla} \times A = -\sigma\frac{\partial \vec{A}}{\partial t} - \sigma\vec{\nabla}\phi + \vec{J_s} \tag{10}$$

Note that (10) is a second order vector diffusion equation for the vector potential $\vec{A}$. At present the scalar potential ϕ is not specified, so in order to reduce ambiguity we enforce the gauge condition

$$\vec{\nabla} \cdot \sigma\vec{A} = 0 \tag{11}$$

This gauge is equivalent to the Coulomb gauge $\vec{\nabla} \cdot \vec{A} = 0$ in regions where σ is constant, but it is different in regions where σ is inhomogeneous. Taking the divergence of (10),enforcing the gauge condition of (11), and assuming the independent current is divergence-free, yields

$$\vec{\nabla} \cdot \sigma\vec{\nabla}\phi = 0 \tag{12}$$

which is a Poisson equation for the scalar potential ϕ. Therefore, if ϕ satisfies Poisson's equation, then the gauge condition of $\vec{A}$ is also satisfied for all time if it is satisfied initially.

Equations (12) and (10) form a complete system for determining the scalar potential ϕ and the vector potential $\vec{A}$ in the domain Ω for all time given a collection of voltage and current sources (e.g. the $\vec{A}$-ϕ potential formulation of [22]). Alternatively, we can formulate a system with the vector state variable $\vec{B}$ in place of $\vec{A}$ by incorporating Faraday's law (2) and taking into account our decomposition of the electric field (9) to write (10) as a set of two coupled equations

$$\sigma\vec{E}^{ind} = \vec{\nabla} \times \frac{1}{\mu}\vec{B} + \sigma\vec{\nabla}\phi - \vec{J_s} \tag{13}$$

$$\frac{\partial \vec{B}}{\partial t} = -\vec{\nabla} \times \vec{E}^{ind} \tag{14}$$

The two formulations (10) and (13)-(14) are equivalent, the former is preferred for analytical analysis while the latter is more amenable for numerical implementation of advection, as discussed in more detail in Section 5.

3 Dynamo Equation

We now consider electromagnetic diffusion in moving materials. We first consider the Eulerian case in which the material positions and field components are defined with respect to the fixed laboratory coordinate system. Let $\vec{x} = \{x_1, x_2, x_3\} \in \mathcal{E}$ denote the label of a point in Euclidean space $\mathcal{E}$ where the motion takes place. The coordinate system of $\mathcal{E}$ is called the *spatial* or *laboratory* system. Let each point in the material be labeled with $\vec{X} = \{X_1, X_2, X_3\} \in \mathcal{M}$. The coordinate system of $\mathcal{M}$ is the *material* system. We assume there exists a time dependent, bijective mapping which relates these two different labels of the same point,

$$\vec{x} = \vec{x}(\vec{X}, t),\ \vec{X} = \vec{X}(\vec{x}, t) \tag{15}$$

While not necessary, it is common to have these two coordinate systems be equal at time $t = 0$, the undeformed state. Let a vector field defined with respect to the laboratory frame be denoted with a prime, e.g. $F'(x,t)$, and the same vector field defined with respect to the material frame be unprimed, e.g. $F(X,t)$. In an Eulerian representation, the fields and operators of a partial differential equation (PDE) are functions of the fixed laboratory frame; in a Lagrangian representation the fields and operators of a PDE are functions of the moving material frame.

Faraday's law (2) can can be written in integral form as

$$\frac{d}{dt}\int_{\Omega(t)} \vec{B}' \cdot da' = -\oint_{\Gamma(t)} \vec{E}' \cdot dl'$$

where the surface $\Omega(t)$ is moving with the material. The material derivative $\frac{d\vec{F}'}{dt}$ of any flux-type quantity $\vec{F}$ is defined as

$$\frac{d}{dt}\int_{\Omega(t)} \vec{F}' \cdot da' = \int_{\Omega(t)} \frac{d\vec{F}'}{dt} \cdot da'$$

and, as shown in [23] and [24], a careful derivation gives

$$\frac{d\vec{F}'}{dt} = \frac{\partial \vec{F}'}{\partial t} - \vec{\nabla} \times \vec{v}' \times \vec{F}' + \vec{v}'(\vec{\nabla} \cdot \vec{F}') \tag{16}$$

where the velocity of a material point $\vec{X}$ on the surface of integration is $\vec{v}' = d\vec{x}/dt$. This material derivative agrees with the so-called total derivative

$$\frac{d\vec{F}'}{dt} = \frac{\partial \vec{F}'}{\partial t} + \vec{v}' \cdot (\vec{\nabla} \otimes \vec{F}')$$

only for the special case of rectilinear motion. Combining (16) with (13)-(14) yields

the dynamo equation

$$\frac{\partial \vec{B}'}{\partial t} = -\vec{\nabla} \times \frac{1}{\sigma\mu}\vec{\nabla} \times \vec{B}' + \vec{\nabla} \times \vec{v} \times \vec{B}' \tag{17}$$

where the source terms $\vec{J_s}$ and $\sigma\vec{\nabla}\phi$ have been discarded for clarity. The first term on the right is diffusion, the second term is advection, and the ratio of these is the magnetic Reynolds number $MRe = \frac{vL}{\lambda}$ where L is the characteristic size and $\lambda \equiv \frac{1}{\sigma\mu}$ is the magnetic diffusivity. For problems in which $MRe \approx 1$ and the velocity is such that advection and diffusion have opposite signs, we have near equilibrium $\frac{\partial \vec{B}'}{\partial t} \approx 0$ and time integration of the dynamo equation requires special care. However, for advection or diffusion dominated problems it is acceptable to employ an operator-splitting of the equation. Let the dynamo equation be represented as

$$\frac{\partial \vec{B}}{\partial t} = L_\sigma(\vec{B}) + L_v(\vec{B})$$

where the operator L_σ denotes electromagnetic diffusion and the operator L_v denotes magnetic advection and consider the two separate equations

$$\frac{\partial \vec{B}_\sigma}{\partial t} = L_\sigma(\vec{B}_\sigma)$$
$$\frac{\partial \vec{B}_v}{\partial t} = L_v(\vec{B}_v)$$

Let $\mathcal{S}_\sigma$ denote the electromagnetic diffusion time integration operator that takes the field $\vec{B}_\sigma$ from a discrete time step n to time step $n+1$, and let $\mathcal{S}_v$ denote the magnetic advection time integration operator that takes $\vec{B}_v$ from a discrete time step n to time $n+1$. The generic operator splitting of the dynamo equation is then given by the composition

$$\vec{B}_{n+1} = [\mathcal{S}_\sigma \circ \mathcal{S}_v]\,\vec{B}^n$$

For this simple operator splitting the time accuracy is $O(\Delta t)$, but numerous alternatives exist that are $O(\Delta t^2)$ or better. The advantage of operator splitting is that different time integration can be used for $\mathcal{S}_\sigma$ and $\mathcal{S}_v$. For example several small explicit steps can be used for the advection operation $\mathcal{S}_v$ while a single large implicit step is used for the diffusion calculation of $\mathcal{S}_\sigma$, a process referred to as sub-cycling. Another key advantage is in terms of software; it is relatively straight forward to add an additional physics "package" to a multi-physics code if the multi-physics code is based on operator splitting. This is the case for ALE3D. Our approach for the dynamo equation is to perform diffusion in the Lagrangian system using implicit time integration, followed by updating the momentum equation in the Lagrangian system explicitly, followed by an optional mesh relaxation and advection step if the mesh becomes too distorted.

3.1 Material Frame

If $\vec{A}$ is a vector in the material coordinate system $\mathcal{M}$ and $\vec{a}$ is the same vector in the laboratory system $\mathcal{L}$, then the components of these vectors are related by

$$a^i = \frac{\partial x^i}{\partial X^j} A^j$$

However, electromagnetic fields and fluxes do not simply transform as vectors. As shown in [23] and [24], voltage and flux are invariants with respect to the deformation transformation

$$\begin{array}{lcc} Material\ \ (Lagrangian) & & Laboratory\ \ (Eulerian) \\ \vec{E}\cdot d\vec{x} & = & (\vec{E}' + \vec{v}' \times \vec{B}')\cdot d\vec{x}' \\ \vec{B}\cdot d\vec{a} & = & \vec{B}'\cdot d\vec{a}' \end{array} \tag{18}$$

Differential arc length and surface area elements transform according to

$$d\vec{x} = J^T d\vec{x}' \tag{19}$$

$$d\vec{a} = |J| J^{-1} d\vec{a}' \tag{20}$$

where our definition of the Jacobian matrix is $J_{ij} = \partial X_j / \partial x_i$. As a consequence, the electric field intensities and magnetic flux densities transform in a dual manner in order to maintain the invariance property of (18)

$$\vec{E} = J^{-1}(\vec{E}' + \vec{v}' \times \vec{B}') \tag{21}$$

$$\vec{B} = \frac{1}{|J|} J^T \vec{B}' \tag{22}$$

In the material system the dynamo equation becomes

$$\frac{\partial \vec{B}}{\partial t} = -\nabla \times \frac{1}{\sigma\mu} \nabla \times \vec{B} \tag{23}$$

where it is understood that the *Curl* operator is with respect to the material coordinate system. Thus the form of the diffusion equation is invariant to material motion when the fields and operators are defined in the material frame. For the special case of a perfectly conducting material this equation gives $\frac{\partial \vec{B}}{\partial t} = 0$, the frozen-in-flux theorem. The operator splitting of the dynamo equation is particularly simple in the material frame: the first step is diffusion of the fields, the second step is to move the mesh nodes according to the resulting $\vec{J} \times \vec{B}$ force while maintaining $\frac{d\vec{B}}{dt} = 0$ during the mesh motion. When a mixed $H(Curl)$ - $H(Div)$ discretization is used for the equations, this latter step means that the magnetic degrees-of-freedom, which represent the net fluxes through each face of the mesh, are constant.

3.2 Mixed Variational Formulation and Time Discretization

Our particular mixed variational formulation is derived from a combination of methods originally presented in [25] and [22]. Our goal is to obtain a numerical formulation where the primary discrete field is the magnetic flux density as found in the $\vec{B}$ field formulation of [25] and where the discrete time integration is performed using a generalized Crank-Nicolson method as found in the $\vec{A}$-ϕ potential formulation of [22]. The advantage of the $\vec{B}$ formulation of [25] becomes apparent during the advection phase of the ALE formulation, as magnetic flux is the best electromagnetic quantity to use for magnetic transport [26]. The advantages of the $\vec{A}$-ϕ potential formulation of [22] are that it can be up to 2nd order accurate in time, and voltage sources can be explicitly added to a problem by specifying them as essential boundary conditions on the additional elliptic PDE, making this method well suited for coupling to an external RLC circuit model.

We begin by decomposing the electric field in Ampere's law (1) according to (9). Now we multiply Ampere's law (1) by a 1-form test function $\vec{W}^1 \in H(Curl)$ and integrate over the three dimensional problem domain Ω to obtain the variational form

$$\int_\Omega \vec{\nabla} \times \frac{1}{\mu}\vec{B} \cdot \vec{W}^1 \, d\Omega = \int_\Omega \sigma(\vec{E}^{irr} + \vec{E}^{ind}) \cdot \vec{W}^1 d\Omega + \int_\Omega \vec{J}_s \cdot \vec{W}^1 d\Omega \tag{24}$$

Now we perform integration by parts on (24), apply the Gauss divergence theorem and move the resulting surface integral term to the right hand side to obtain

$$\begin{aligned} &\int_\Omega \frac{1}{\mu}\vec{B} \cdot \vec{\nabla} \times \vec{W}^1 \, d\Omega = \\ &\quad \int_\Omega \sigma(\vec{E}^{irr} + \vec{E}^{ind}) \cdot \vec{W}^1 d\Omega + \int_\Omega \vec{J}_s \cdot \vec{W}^1 d\Omega + \oint_\Gamma \hat{n} \times \frac{1}{\mu}\vec{B} \cdot \vec{W}^1 \, d\Gamma \end{aligned} \tag{25}$$

Now we assume that the fields $\vec{E}$ and $\vec{B}$ are known at discrete time intervals denoted by the subscript integer n. We apply a generalized trapezoidal approximation for the time derivative of the magnetic field such that

$$\vec{B}_{n+1} = \vec{B}_n + (1-\alpha)\Delta t \frac{\partial \vec{B}}{\partial t}|_n + \alpha \Delta t \frac{\partial \vec{B}}{\partial t}|_{n+1} \tag{26}$$

The averaging parameter α determines the nature of the numerical time integration such that

$$\alpha = \begin{cases} 0 & \text{Explicit, 1st Order Accurate Forward Euler} \\ 1/2 & \text{Implicit, 2nd Order Accurate Crank Nicolson} \\ 1 & \text{Implicit, 1st Order Accurate Backward Euler} \end{cases}$$

Applying this discretization to Faraday's law (2), we obtain

$$\vec{B}_{n+1} = \vec{B}_n - \Delta t \vec{\nabla} \times \left((1-\alpha)\vec{E}_n^{ind} + \alpha \vec{E}_{n+1}^{ind} \right) \tag{27}$$

Now we substitute $\vec{B}$ on the left hand side of (25) with the expression for $\vec{B}_{n+1}$ from (27), moving all quantities at time step n to the right hand side of the equation to obtain

$$\begin{aligned} &\alpha \Delta t \int_\Omega \frac{1}{\mu} \vec{\nabla} \times \vec{E}_{n+1}^{ind} \cdot \vec{\nabla} \times \vec{W}^1 \, d\Omega = \\ &\int_\Omega \frac{1}{\mu} \vec{B}_n \cdot \vec{\nabla} \times W^1 \, d\Omega - (1-\alpha)\Delta t \int_\Omega \frac{1}{\mu} \vec{\nabla} \times \vec{E}_n^{ind} \cdot \vec{\nabla} \times \vec{W}^1 \, d\Omega \\ &- \int_\Omega \sigma (\vec{E}_{n+1}^{irr} + \vec{E}_{n+1}^{ind}) \cdot \vec{W}^1 \, d\Omega - \int_\Omega \vec{J}_s \cdot \vec{W}^1 \, d\Omega - \oint_\Gamma \hat{n} \times \frac{1}{\mu} \vec{B} \cdot \vec{W}^1 \, d\Gamma \end{aligned} \tag{28}$$

where we have added the time step subscript $n+1$ to the fields $\vec{E}^{irr}$ and $\vec{E}^{ind}$ on the right hand side. We introduce a secondary variable, $\tilde{\vec{B}}$, defined as

$$\tilde{\vec{B}}_n \equiv \vec{B}_n - (1-\alpha)\Delta t \vec{\nabla} \times \vec{E}_n^{ind} \tag{29}$$

Now we rewrite (28) in terms of our new secondary variable $\tilde{\vec{B}}$ while making the substitution $\vec{E}^{irr} = -\vec{\nabla}\phi$, and after rearranging terms we obtain

$$\begin{aligned} &\int_\Omega \sigma \vec{E}_{n+1}^{ind} \cdot \vec{W}^1 d\Omega + \int_\Omega \alpha \Delta t \vec{\nabla} \times E_{n+1}^{ind} \cdot \vec{\nabla} \times \vec{W}^1 \, d\Omega = \\ &\int_\Omega \frac{1}{\mu} \tilde{\vec{B}}_n \cdot \vec{\nabla} \times \vec{W}^1 \, d\Omega + \int_\Omega \sigma \vec{\nabla} \phi_{n+1} \cdot \vec{W}^1 \, d\Omega - \int_\Omega \vec{J}_s \cdot \vec{W}^1 \, d\Omega \\ &- \oint_\Gamma \hat{n} \times \frac{1}{\mu} \vec{B} \cdot \vec{W}^1 \, d\Gamma \end{aligned} \tag{30}$$

The natural and essential boundary conditions for (30) are

$$\begin{aligned} Natural \quad \hat{n} \times \tfrac{1}{\mu} \vec{B} &= 0 \text{ ``Neumann''} \\ Essential \ \hat{n} \times \vec{E}^{ind} &= 0 \text{ ``Dirichlet''} \end{aligned} \tag{31}$$

In other words, the tangential magnetic field $\vec{H}$ is the natural boundary condition while the tangential induced electric field $\vec{E}^{ind}$ is the essential boundary condition. Recall that the *essential* boundary condition is a constraint that is enforced manually, whereas the *natural* boundary condition is satisfied in the variational (weak) sense. In general, the inhomogeneous versions of these two boundary conditions require vector valued functions $\vec{g}_N(\Gamma)$ and $\vec{g}_D(\Gamma)$ such that

$$\hat{n} \times \frac{1}{\mu}\vec{B} = \vec{g}_N \text{ on } \Gamma_N$$
$$\hat{n} \times \vec{E} = \vec{g}_D \text{ on } \Gamma_D$$

Note that the variational formulation of (30) is incomplete due to the presence of the ϕ_{n+1} term on the right hand side. In order to fully define the problem, we must add an additional variational equation to define the scalar potential. To do this, we multiply (12) by a scalar 0-form test function $W^0 \in H(Grad)$ and integrate over the domain Ω

$$\int_\Omega (\vec{\nabla} \cdot \sigma \vec{\nabla} \phi)\, W^0 \, d\Omega = 0$$

and employ Green's first scalar identity to obtain

$$\int_\Omega \sigma \vec{\nabla} \phi \cdot \vec{\nabla} W^0 \, d\Omega = \oint_\Gamma \hat{n} \cdot \sigma \vec{\nabla} \phi \, W^0 \, d\Gamma \tag{32}$$

for all test function W^0. For this variational equation, the *natural* and *essential* boundary conditions are

$$\begin{aligned} Natural \quad \hat{n} \cdot \sigma \vec{\nabla} \phi &= 0 \text{ ``}Neumann'' \\ Essential \quad \phi &= 0 \text{ ``}Dirichlet'' \end{aligned} \tag{33}$$

In other words, the normal component of the conduction current $\sigma \vec{E}^{irr}$ is the natural boundary condition while the surface scalar potential (or voltage) ϕ is the essential boundary condition. In general, the inhomogeneous versions of these two boundary conditions require scalar valued functions $g_N(\Gamma)$ and $g_D(\Gamma)$ such that

$$\hat{n} \cdot \sigma \vec{\nabla} \phi = g_N \text{ on } \Gamma_N$$
$$\phi = g_D \text{ on } \Gamma_D$$

3.3 Mixed Finite Element Discretization

We assume the three dimensional domain Ω has been partitioned into a set of discrete hexahedral elements Σ_i, the union of which forms the finite element mesh Ω_h. Furthermore, we assume the surface boundary Γ has been partitioned into the sets Γ_N and Γ_D, denoting surfaces to which either a Neumann (*Natural*) or Dirichlet (*Essential*) boundary condition is applied.

We will discretize the variational form of the coupled magnetic dynamo equations of (30) and (32) using a mixed finite element method. In the context of Galerkin approximations, the choice of the finite element space plays a crucial role in the

stability and convergence of the discretization. For the case of Maxwell's equations, mixed finite element methods which use $H(Curl)$ and $H(Div)$ conforming spaces to model the electric field intensities and magnetic flux densities respectively are preferred over traditional nodal vector spaces since they eliminate spurious modes in eigenvalue computations and they prevent fictitious charge build-up in time-dependent computations. Furthermore, as shown in [27], the $H(Curl)$ and $H(Div)$ conforming methods satisfy the transformation properties of (21) and (22) in a discrete sense, making them well suited for an ALE treatment of MHD. For further information regarding the use of $H(Curl)$ and $H(Div)$ finite elements (aka vector finite elements, "edge" and "face" elements, discrete differential forms) for Maxwell's equations, the reader is referred to [22], [28], [27], [29], [30], [25] [31].

In our proposed ALE formulation the scalar potential ϕ will be discretized on element nodes (i.e. a discrete 0-form field of polynomial degree $p = 1$), the electric field will be discretized on element edges (i.e. a discrete 1-form field of polynomial degree $p = 1$) and the magnetic flux density $\vec{B}$ will be discretized on element faces (i.e. a discrete 2-form field of polynomial degree $p = 1$). For a hexahedral element in the Lagrangian frame we have

$$\phi(\vec{X},t) \approx \sum_{i=1}^{8} v_i(t) W_i^0(\vec{X}), \quad W^0 \in H(Grad) \tag{34}$$

$$\vec{E}(\vec{X},t) \approx \sum_{i=1}^{12} e_i(t) \vec{W}_i^1(\vec{X}), \quad \vec{W}^1 \in H(Curl) \tag{35}$$

$$\vec{B}(\vec{X},t) \approx \sum_{i=1}^{6} b_i(t) \vec{W}_i^2(\vec{X}), \quad \vec{W}^2 \in H(Div) \tag{36}$$

where the integer superscript on the basis function is the degree of the discrete differential form. For the case of (34), the degrees of freedom $v_i(t)$ are time dependent voltages at element nodes and the basis functions are unit-less. For the case of (35), the degrees of freedom $e_i(t)$ are time dependent induced voltages along element edges and the basis functions have units of inverse distance. Finally, for the case of (36), the degrees of freedom $b_i(t)$ are time dependent magnetic fluxes through element faces and the basis functions have units of inverse area.

We employ the finite element library FEMSTER [32], [22] for computation of the local "mass", "stiffness", and "derivative" matrices, where γ denotes an arbitrary symmetric tensor function of time and space (for material constitutive relations) and the superscript $l = 0,1,2,3$ denotes the degree of the form

$$\mathbf{M}^l(\gamma)_{ij} = \int_\Omega \gamma W_i^l \, W_j^l \, d\Omega \tag{37}$$

$$\mathbf{S}^l(\gamma)_{ij} = \int_\Omega \gamma dW_i^l \cdot dW_j^l \, d\Omega \tag{38}$$

$$\mathbf{D}^{l(l+1)}(\gamma)_{ij} = \int_\Omega \gamma dW_i^l \cdot W_j^{l+1} \, d\Omega \tag{39}$$

Note that the d operator denotes *Gradient, Curl*, or *Divergence*, for $l = 0,1,2$ respectively. The "mass" matrices $\mathbf{M}$ and the "stiffness" matrices $\mathbf{S}$ are square and map l-forms to l-forms, the "derivative" matrices $\mathbf{D}$ are rectangular and map l-forms to $(l+1)$-forms. It can be shown that

$$\mathbf{D}^{l(l+1)} = \mathbf{M}^{l+1}\mathbf{K}^{l(l+1)} \tag{40}$$

$$\mathbf{S}^l = \left(\mathbf{K}^{l(l+1)}\right)^T \mathbf{M}^{l+1}\mathbf{K}^{l(l+1)} \tag{41}$$

$$\tag{42}$$

where $\mathbf{K}^{l(l+1)}$ is a "topological derivative" matrix. This matrix is the discretization of the exterior derivative operator d from differential geometry, $dW^l = W^{(l+1)}$. This matrix depends upon the mesh connectivity, but is independent of the nodal coordinates. It does not involve an integral over the element, and it does not involve any material properties. While seemingly abstract, it is enormously valuable in practice. Given an l-form quantity X with basis function expansion

$$X = \sum_{i=1}^{n} x_i W_i^l, \tag{43}$$

and an $(l+1)$-form quantity Y with basis function expansion

$$Y = \sum_{i=1}^{n} y_i W_i^{(l+1)}, \tag{44}$$

the exterior derivative (*Gradient, Curl, Divergence* for $l = 0,1,2$ respectively) is given by

$$\mathbf{y} = \mathbf{K}^{l(l+1)}\mathbf{x}. \tag{45}$$

It can be shown that

$$\mathbf{K}^{12}\mathbf{K}^{01} = 0 \tag{46}$$

$$\mathbf{K}^{23}\mathbf{K}^{12} = 0 \tag{47}$$

which are the discrete versions of $d(dW^l) = 0$. In terms of standard vector calculus, these matrix relations correspond to the identities $\vec{\nabla} \times \vec{\nabla} f = 0$ and $\vec{\nabla} \cdot \vec{\nabla} \times \vec{F} = 0$, respectively. These identities are satisfied in the discrete sense, exactly (to machine precision), for any mesh and any order basis function. While FEMSTER supports arbitrary order elements, basis functions, and quadratures, only linear basis functions will be employed here.

Using the matrix notation previously defined, we can now write the fully discrete formulation of the magnetic dynamo equation in the Lagrangian frame as

$$\mathbf{S}^0\mathbf{v}_{n+1} = \mathbf{g}^0 \tag{48}$$

$$\left(\mathbf{M}^1(\sigma) + \alpha\Delta t\mathbf{S}^1(\mu^{-1})\right)\mathbf{e}^{ind}_{n+1} = (\mathbf{D}^{12}(\mu^{-1}))^T\tilde{\mathbf{b}}_n + \mathbf{D}^{01}(\sigma)\mathbf{v}_{n+1} - \mathbf{f}^1 - \mathbf{g}^1 \tag{49}$$

$$\mathbf{b}_{n+1} = \tilde{\mathbf{b}}_n - \alpha\Delta t\mathbf{K}^{12}\mathbf{e}_{n+1} \tag{50}$$

$$\tilde{\mathbf{b}}_{n+1} = \mathbf{b}_{n+1} - (1-\alpha)\Delta t\mathbf{K}^{12}\mathbf{e}_{n+1} \tag{51}$$

where $\mathbf{v}$ is an array consisting of the time dependent voltage degrees of freedom from the scalar potential solve of (34) for every node in the mesh, $\mathbf{e}^{ind}$ is an array consisting of the time dependent induced voltage degrees of freedom of (35) for every edge in the mesh, $\mathbf{b}$ is an array consisting of the time dependent magnetic flux degrees of freedom of (36) for every face in the mesh, $\mathbf{f}^1$ is a volume current source term and $\mathbf{g}^1$ is a surface source term. Note that the face based array $\tilde{\mathbf{b}}$, the discrete analog of the secondary variable we introduced in (29), is the only state variable required to be known at time n. This is a critical feature of our discretization; it means the only state variable that needs to be remapped during our Eulerian advection phase in Section 5 is this face based time averaged flux.

Note that in (49) the rectangular derivative matrices $\mathbf{D}^{12}(\mu^{-1})$ and $\mathbf{D}^{01}(\sigma)$ are discrete versions of the *Curl* and *Gradient* defined with respect to the Lagrangian frame (i.e. they have metric information encoded in them by virtue of the mass matrix). As such, they will change as the mesh is moved by $\vec{J}\times\vec{B}$ forces. Furthermore, the discrete divergence constraints on the fields are given by

$$\left(\mathbf{D}^{01}(\sigma)\right)^T\mathbf{e} = 0 \tag{52}$$

$$\mathbf{K}^{23}\mathbf{b} = 0 \tag{53}$$

and from the identities (46) and (47) these constraints are implicitly satisfied for all time, assuming the initial conditions and the source terms are divergence free.

4 Lagrangian Motion

In this section we review methods for coupling the electromagnetic force and heat terms to the equations of Lagrangian motion. This phase of the calculation can be viewed as the Lagrangian treatment of the advection operator L_v of the magnetic dynamo equation. Given an electromagnetic force, we move the mesh nodes according to this force, keeping the magnetic degrees-of-freedom (face fluxes) constant. The new node locations affect the basis functions, so while the magnetic degrees-of-freedom are constant the magnetic field is in fact properly advected. We begin

with the general continuum equation of motion derived from Newton's second law. In a co-moving (or Lagrangian) reference frame, this is given by

$$\rho \frac{\partial^2 \vec{u}}{\partial t^2} = \vec{\nabla} \cdot \overleftrightarrow{S} + \vec{F} \tag{54}$$

where ρ is the material mass density, $\vec{u}$ is the displacement vector, $\overleftrightarrow{S}$ is the Cauchy stress tensor, and $\vec{F}$ is an independent volumetric body force density. The variational form of (54) is constructed by multiplying by a test vector $\vec{w}$ and integrating over the entire domain Ω

$$\frac{\partial^2}{\partial t^2} \int_\Omega \rho \vec{u} \cdot \vec{w} \, d\Omega = \int_\Omega \left(\vec{\nabla} \cdot \overleftrightarrow{S} \right) \cdot \vec{w} \, d\Omega + \int_\Omega \vec{F} \cdot \vec{w} \, d\Omega \tag{55}$$

If the test vector $\vec{w}$ is considered to have units of distance, then each term in the above equation has units of work; hence this variational method is often referred to as the method of virtual work. For a valid variational method, each component of the test vector w_i must be a fully continuous function, i.e. $w_i \in H(Grad)$, and the stress tensor must satisfy certain symmetry conditions. Integration by parts is employed to yield

$$\frac{\partial^2}{\partial t^2} \int_\Omega \rho \vec{u} \cdot \vec{w} \, d\Omega = \int_\Gamma (\overleftrightarrow{S} \cdot \hat{n}) \cdot \vec{w} \, d\Gamma - \int_\Omega \overleftrightarrow{S} : (\vec{\nabla} \otimes \vec{w}) \, d\Omega + \int_\Omega \vec{F} \cdot \vec{w} \, d\Omega \tag{56}$$

where $\hat{n}$ is the outward normal of the surface Γ. The common boundary conditions are the *displacement* (Dirichlet, essential) condition $\vec{u} = \vec{d}$ on Γ and the *traction* (Neumann, natural) condition $\overleftrightarrow{S} \cdot \hat{n} = \vec{t}$ on Γ. Furthermore, we decompose the stress tensor into a sum of deviatoric and hydrostatic components such that

$$S_{ij} = \tau_{ij} - P\delta_{ij} \tag{57}$$

where P is the hydrostatic pressure defined to be the mean of the principle stresses $P = \frac{1}{3} S_{ii}$, and δ_{ij} is the Kronecker delta. The deviatoric stress components τ_{ij} are primarily determined by a material's constitutive models while the hydrostatic components are determined by the material's equation of state (EOS), i.e. a material's pressure as a function of energy or temperature.

4.1 Computation of Electromagnetic Force

There are multiple options for coupling the electromagnetic force to the elastic equation of motion (54). The conceptually simplest approach is to compute $\vec{F} = \vec{J} \times \vec{B}$ and use this as the body force in (55). As shown in [23], the $\vec{J} \times \vec{B}$ body force density is equivalent to the divergence of a Maxwell stress tensor plus a term

involving the divergence of $\vec{B}$ such that

$$\vec{J} \times \vec{B} = \frac{1}{\mu}\vec{B} \cdot (\vec{\nabla} \otimes \vec{B}) - \vec{\nabla}(\frac{|B|}{2\mu}) = \vec{\nabla} \cdot \overleftrightarrow{T} - \vec{B}(\vec{\nabla} \cdot \vec{B})$$

Under the good conductor approximation of (6) (i.e. ignoring energy stored in displacement current), the Maxwell stress tensor (MST) is given by

$$T_{ij} = \frac{1}{\mu}\left(B_i B_j - \frac{1}{2}\delta_{ij} B_k B_k\right) \tag{58}$$

Provided that $\vec{\nabla} \cdot \vec{B} = 0$ (implying no forces due to the presence of magnetic charge), then the $\vec{J} \times \vec{B}$ body force and the MST approach will yield identical accelerations of a conducting body. It is interesting to point out the similarities between the Cauchy stress tensor decomposition of (57) and the Maxwell stress tensor of (58). The MST consists of a deviatoric component $\frac{1}{\mu}B_i B_j$ and a pressure component consisting of the principle Maxwell stresses $\frac{1}{2}\delta_{ij} B_k B_k$. For MHD problems, the mean of the principle Maxwell stress terms is equivalent to the magnetic pressure $\frac{1}{2\mu}|\vec{B}|^2$. The deviatoric components of the MST can add an effective "magnetic strength" to materials that might otherwise have no strength. This gives rise to the physical phenomena of shear Alfven waves, an example of which is given in Section 6. From a discretization standpoint it is very straightforward to implement the MST approach. We simply evaluate the components of (58) at element quadrature points in the Lagrangian frame at the discrete time level $n+1$ via the face based representation of (36) and add these values to the corresponding component of the Cauchy stress tensor in the discretization of (56). This is consistent with the time centering of the hydrodynamic variables in ALE3D, where the Cauchy stress divergence terms (which are used to compute accelerations) are known at the discrete time step $n+1$, since stress rates are integrated at $n+\frac{1}{2}$.

4.2 Computation of Resistive Energy Loss

Due to the resistive nature of the coupled magnetic dynamo equations of (13) and (14), the energy stored in the magnetic fields is subject to dissipation due to Joule heating. To account for this energy loss, we need to compute a resistive energy loss term and couple this to the equation of state describing our material models. This can be accomplished by computing the resistive energy loss density

$$e_\sigma = \vec{J} \cdot \vec{E} = \sigma\vec{E} \cdot \vec{E} = \sigma(\vec{E}^{ind} - \vec{\nabla}\phi) \cdot (\vec{E}^{ind} - \vec{\nabla}\phi) \tag{59}$$

Again, from a discretization standpoint it is very straightforward to implement the resistive energy loss term. We simply evaluate the term of (59) at element centroids at the discrete time level $n+1$ via the edge based representation of (35) and the node based representation of (34) and add these values to existing zonal energies at

time $n+1$, which is consistent with the time centering of energy density variables in ALE3D.

5 Eulerian Advection

The ALE3D code performs an optional equipotential relaxation of the mesh. This is important for problems with gross deformation of the mesh, it prevents the mesh from becoming tangled. If relaxation is performed, fields defined on the "old" mesh must be remapped to the "new" mesh. This remapping is equivalent to Eulerian advection, but with a fictitious mesh velocity $\vec{v}_m$. It is interesting to note that it is possible to implement a pure Eulerian formulation as a Lagrange step followed by a complete remap step in which the mesh snaps back to its original configuration at every time step. We consider only new grids which are "nearby" in the sense that only small perturbations of the grid are allowed (i.e. the mesh nodes should not travel farther than one mesh element in any one relaxation step). This is known as the continuous remap approximation (CRA). This is in contrast to general remapping methods (a.k.a. interpolation methods, see [33]) whose goal is to remap quantities between two arbitrary grids. Under the CRA, the nodes of the old mesh are displaced to new locations; the topology (or connectivity) of the mesh does not change. Furthermore we restrict the relaxation process to interior mesh nodes, keeping all boundary nodes fixed. A key point is that the divergence of the magnetic flux density should be preserved during the advection process, this is referred to as constrained transport or constrained interpolation. The definition of the Maxwell stress tensor assumes a zero divergence field, so if the advection step does not preserve divergence then some additional post processing (projection, filtering) would be required to prohibit unlimited growth of magnetic monopoles and the resulting non-physical forces.

5.1 Constrained Transport of Magnetic Flux

Once again we assume the frozen flux condition (the diffusion of the fields has already been computed) and now our goal is to compute the rate of change of the magnetic flux density due to advective "transport" caused by the mesh motion. In essence, we are holding the magnetic field $\vec{B}$ fixed in space and letting the mesh relax around it; this is opposite in sense to advecting a magnetic field across a fixed Eulerian mesh (as is the case with the original CT method of [12]). The change in magnetic flux density due to mesh relaxation is therefore

$$\frac{\partial}{\partial t}\vec{B} = -\vec{\nabla} \times \vec{v}_m \times \vec{B} \tag{60}$$

where v_m denotes the mesh velocity. It is imperative that this process maintain the solenoidal nature of the $\vec{B}$ field by satisfying the constraint

$$\vec{\nabla} \cdot \vec{B} = 0.$$

Now consider an arbitrarily oriented surface S with differential surface area $d\vec{a}$. We integrate (60) over the surface S

$$\int_S \frac{\partial}{\partial t} \vec{B} \cdot d\vec{a} = -\int_S \vec{\nabla} \times (\vec{v}_m \times \vec{B}) \cdot d\vec{a}$$

Now we apply Stokes' theorem to obtain

$$\frac{\partial \Phi}{\partial t} = -\oint_C (\vec{v}_m \times \vec{B}) \cdot d\vec{x} \tag{61}$$

where Φ denotes total magnetic flux through the surface S, and C represents the boundary of the surface S with differential arc length $d\vec{x}$. Equation (61) states that a voltage in a circuit loop C is induced by a time rate of change of flux through this loop due to the motion of the mesh across the "frozen-in" $\vec{B}$ field.

Now suppose the surface S, in the presence of a fixed background $\vec{B}$ field, moves arbitrarily (including distortion, stretching, re-orientation, etc ...) in a time Δt_m. We can approximate the time derivative for the magnetic flux using a simple finite difference

$$\frac{\partial \Phi}{\partial t} \approx \frac{\Phi^{new} - \Phi^{old}}{\Delta t_m}$$

where Φ^{old} is the flux through the original surface S at time t and Φ^{new} is the flux through the surface S at time $t + \Delta t_m$. We know from a Taylor series analysis that this simple finite difference will be second order accurate if $\frac{\partial \Phi}{\partial t}$ is known at time $t + \frac{1}{2}\Delta t_m$. This provides us with a numerical method for computing the new flux

$$\Phi^{new} \approx \Phi^{old} - \Delta t_m \oint_C (\frac{\vec{u}}{\Delta t_m} \times \vec{B}) \cdot d\vec{x} \;=\; \Phi^{old} - \oint_C (\vec{u} \times \vec{B}) \cdot d\vec{x} \tag{62}$$

where $\vec{u} = \Delta t_m \vec{v}_m$ is the displacement of the surface S. Stated another way, we can approximate the flux through the new surface by "measuring" the voltage in the closed circuit loop C. This approximation is most accurate if the location of the loop C is halfway between the old face and the new face. See Figure 1 for a depiction of this.

5.2 Algebraic Constrained Transport on 3D Unstructured Grids

Let $\vec{x}^{old}$ denote the positions of the mesh nodes after a Lagrangian time step and let $\vec{x}^{new}$ denote the mesh nodes after one mesh relaxation step. We define the nodal

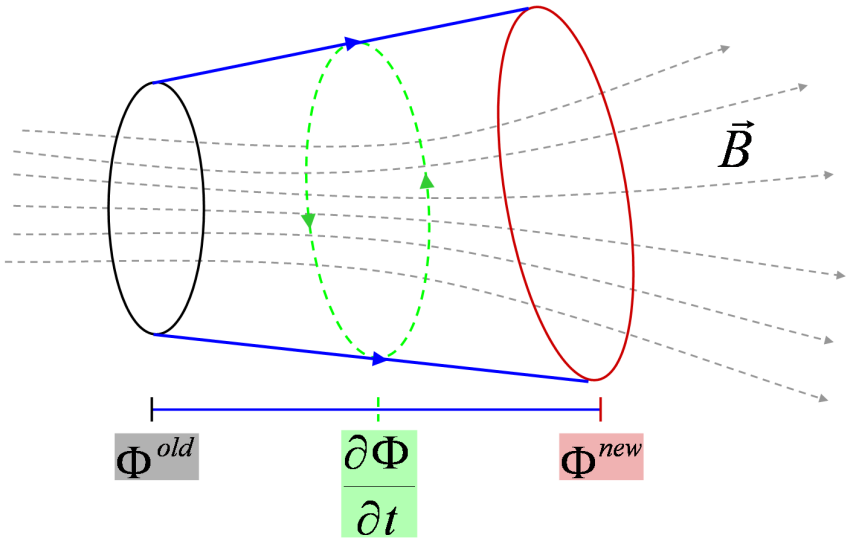

Fig. 1. Schematic diagram depicting the relationship between magnetic flux through two arbitrary faces and the corresponding time rate of change of magnetic flux.

displacement as

$$\vec{u} \equiv \vec{x}^{new} - \vec{x}^{old} \tag{63}$$

Furthermore, we define an intermediate nodal position $\vec{x}^{mid}$ as

$$\vec{x}^{mid} = \vec{x}^{old} + \frac{1}{2}\vec{u} \tag{64}$$

Since the topology (or connectivity) of a mesh is constant for all time, there is a one to one correspondence between mesh entities such as edges and faces at the old, intermediate and new locations. This allows us to define an *intermediate mesh* with unique edges and faces, topologically identical to the old and new faces. These intermediate quantities differ geometrically from their old and new counterparts by virtue of the nodal positions $\vec{x}^{mid}$. A schematic representation of this is shown in Figure 2.

Now suppose we have calculated the magnetic flux density $\vec{B}$ in a Lagrangian time step via the proposed method of (50). Recall that $\vec{B}$ is a 2-form and is approximated by 2-form basis functions according to the expansion

$$\vec{B}^{old} \approx \sum_{i=1}^{6} b_i^{old} \vec{W}_i^{2,old} \tag{65}$$

The degrees of freedom b_i^{old} in this expansion carry the units of magnetic flux; this implies that we know the magnetic flux through every face in the Lagrangian (or old) mesh. Our goal is to compute new values of the magnetic flux b_i^{new} which will

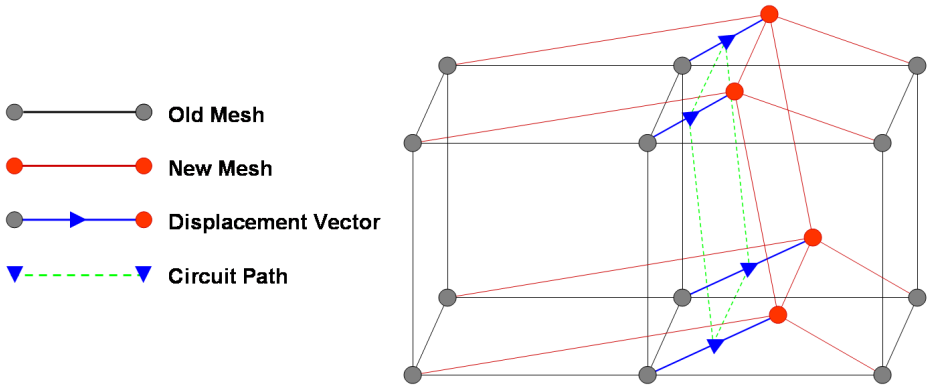

Fig. 2. Schematic diagram depicting a simple two element mesh with one face displaced. Topologically speaking, the old and new meshes are identical. They differ geometrically by the location of the nodes in space. The voltage update circuit is depicted in dashed-green and corresponds to a set of four edges, determined by the four intermediate nodes, which forms the boundary of an intermediate face.

allow us to represent the magnetic flux density on the new mesh as

$$\vec{B}^{new} \approx \sum_{i=1}^{6} b_i^{new} \vec{W}_i^{2,new} \tag{66}$$

where $\vec{W}_i^{2,new}$ denote the basis functions for the new mesh (which are known once the locations of the new mesh nodes are computed).

Using (62) as a starting point, we can compute the flux through a given face in the new mesh by

$$b_i^{new} = b_i^{old} + \Delta b_i \tag{67}$$

The flux change Δb_i we are adding to each face in the old mesh is computed by numerically integrating the voltage along the closed circuit path C, defined by 4 intermediate edges, which in turn are defined by the four intermediate nodes $\vec{x}^{mid}$ associated with each face. Specifically, we can compute the flux change as

$$\Delta b_i = -\sum_{j=1}^{4} \left(\vec{x}_{j+1}^{mid} - \vec{x}_j^{mid} \right) \cdot \left(\frac{(\vec{u}_j \times \vec{B}|_{\vec{x}=\vec{x}_j^{mid}}) + (\vec{u}_{j+i} \times \vec{B}|_{\vec{x}=\vec{x}_{j+1}^{mid}})}{2} \right) \tag{68}$$

where the index j is cyclic (modulo 4). A detailed schematic representation of this is shown in Figure 3. Each term in the sum of (68) is a line integral of the voltage along one of the intermediate edges. This integral is computed with the trapezoid rule. A critical point is that this computation requires evaluation of the magnetic flux density $\vec{B}$ at the intermediate nodes; this process will be discussed in detail in the next section.

The flux update of (68) relies on defining a circulation around the four intermediate

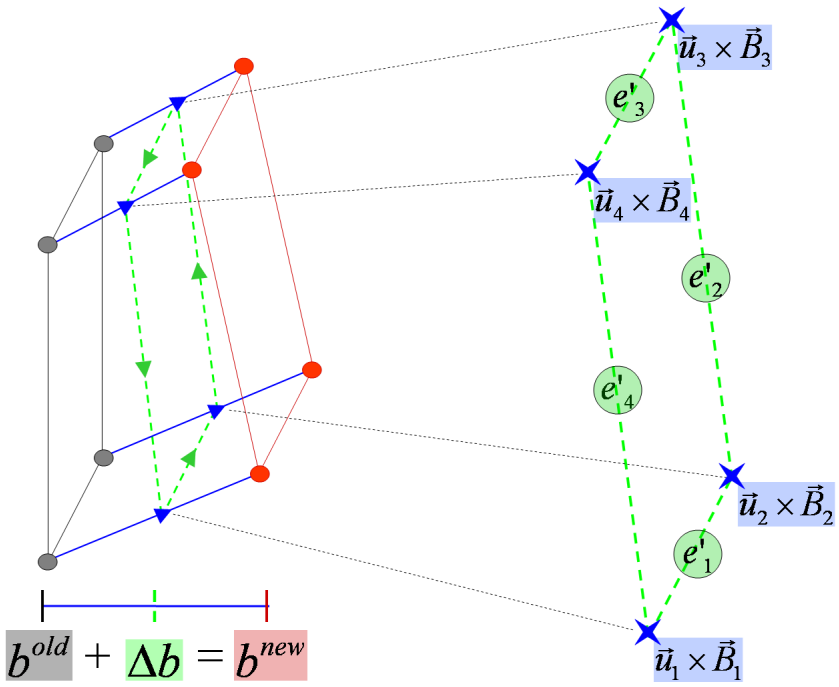

Fig. 3. Schematic diagram detailing the process of computing the update voltage along the closed circuit C defined by four intermediate edges. Given the values of $\vec{u} \times \vec{B}$ at each intermediate node, a voltage contribution from each intermediate edge can be computed. The appropriately signed sum of each edge contribution is the flux change for the face.

edges. The direction of the circulation will determine the sign of Δb. Either of both directions can be used; however, it is imperative that the choice is made consistently in order to compute b_i^{new} for each face. On a general unstructured grid, it can become difficult to enforce such a rule, especially if one has no control over the source of the mesh topology. As such, a more robust (and ultimately more revealing) method for updating the fluxes can be obtained by considering the rectangular topological derivative matrix $\mathbf{K}^{12}$ of (45) (described in detail in [27] and [22]) which is a sparse rectangular matrix representing an incidence map between edges and faces of a mesh. The first step is to introduce an edge based array $\mathbf{e}'$ representing the edge based flux contributions defined by a line integral along that edge. For every edge in the mesh, we have

$$\mathbf{e}'_j = \left(\vec{x}_b^{mid} - \vec{x}_a^{mid}\right) \cdot \left(\frac{\left(\vec{u}_a \times \vec{B}|_{\vec{x}=\vec{x}_a^{mid}}\right) + \left(\vec{u}_b \times \vec{B}|_{\vec{x}=\vec{x}_b^{mid}}\right)}{2} \right) \tag{69}$$

where the generic integers a and b denote the unique integer IDs of the intermediate mesh nodes associated with edge j such that $a < b$. Therefore, the direction of the line integral is uniquely defined according to a global standard like that originally proposed in [27] (i.e. the line integral path is always from the node with low integer ID to the node with high integer ID). We can now write the flux update in terms of

global mesh arrays as

$$\mathbf{b}^{new} = \mathbf{b}^{old} - \mathbf{K}^{12}\mathbf{e}' \tag{70}$$

Written in this form, it is clear that the flux update method will preserve the solenoidal nature of the magnetic field. Taking the discrete divergence of (70) yields

$$\mathbf{K}^{23}\mathbf{b}^{new} = \mathbf{K}^{23}\mathbf{b}^{old} + \mathbf{K}^{23}(\mathbf{K}^{12}\mathbf{e}') = 0 \tag{71}$$

Therefore, the divergence-free constraint is satisfied to machine precision for every mesh relaxation step. Compare the flux update of (70) to the discrete Faraday's law of (50).

5.3 Patch Recovery Process for Nodal Magnetic Field Representation

In order to compute the edge based voltage contributions of (69), we need to evaluate the $\vec{B}$ field at the points $\vec{x}^{mid}$. By virtue of the continuous remap approximation, the points $\vec{x}^{mid}$ are guaranteed to lie inside (or possibly on) an upwind element of the old (or Lagrangian) mesh. An example of this is depicted in Figure 4.

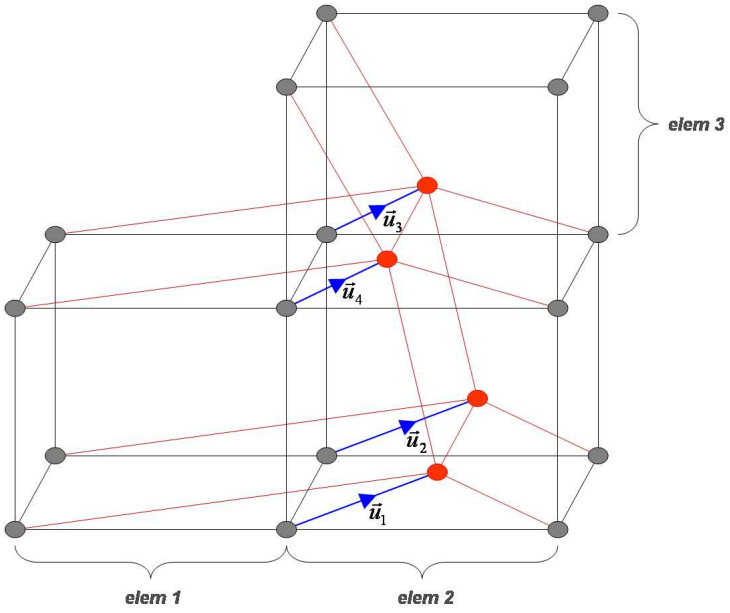

Fig. 4. Schematic diagram depicting the upwind locations of the intermediate mesh nodes $\vec{x}_i^{mid} = \vec{x}_i^{old} + \frac{1}{2}\vec{u}_i$. In this example, $\vec{x}_1^{mid}$ and $\vec{x}_2^{mid}$ lie in element 2 of the old mesh while $\vec{x}_3^{mid}$ and $\vec{x}_4^{mid}$ lie in element 3 of the old mesh

Once the upwind elements are known for each intermediate node, we can use a finite element representation to evaluate $\vec{B}$ inside of the upwind element at the location of the intermediate node $\vec{x}^{mid}$. However, we cannot use the face representation of (36) since, by construction, this representation is tangentially discontinuous across element boundaries. Instead, we perform a type of patch recovery to obtain

a fully continuous (or smooth) representation of $\vec{B}$ which we will denote as $\vec{B}^{avg}$. We define the smooth representation as

$$\vec{B}^{avg} = \sum_{i=1}^{8} \sum_{j=1}^{3} b_{i,j}^{avg} \vec{V}_{i,j} \tag{72}$$

This representation has 24 degrees of freedom, corresponding to three vector components located at each of the 8 element nodes, and is fully continuous at element boundaries. This nodal vector field representation is equivalent to the tri-linear interpolation commonly used for FEM discretization of fluid velocities. The vector valued basis functions $\vec{V}_{i,j}$ can be viewed as 3 sets of 0-form (or scalar nodal) basis functions, one for each component of the vector field.

There are several options for computing the degrees of freedom $b_{i,j}^{avg}$ for this representation. The simplest and most efficient method is to first compute a cell centered value of the magnetic field for every element in the mesh using the face based representation of (36), then to apportion a volume weighted average of this value to each node. This is a cumulative process, any given node will receive a contribution from every element it is connected to. This cumulative nodal value is then divided by a "nodal volume." A more robust, and hence computationally expensive method is to employ the so called Hodge star matrix (see [22] for further details) and solve the following linear system for each component of the averaged nodal values

$$\mathbf{M}^0 b_i^{avg} = (\mathbf{H}^{03})^T b_i^{cc} \tag{73}$$

where $\mathbf{M}^0$ denotes a 0-form mass matrix, $\mathbf{H}^{03}$ is a rectangular Hodge matrix which maps node-centered 0-form quantities to cell-centered 3-form quantities and b^{cc} denotes the cell centered evaluation of the face based representation of (36). In practice, we have found that the simple volume averaging method is sufficient for our needs and is the method we employ for our advection results in Section 6.

5.4 Algebraic Flux Correction for Magnetic Shocks

The transport method of Section 5.2 is second order accurate and will therefore exhibit non-monotonic solution behavior (aka spurious oscillations, "ringing", or overshoots and undershoots) for solutions with discontinuities or shock fronts. We must impose a form of limiting that will suppress the non-monotonic solution behavior. Limiting schemes for the scalar advection equation are prevalent and well understood as a result of many years of research in the computational fluid dynamics (CFD) community [34]. Nevertheless, the design of genuinely multidimensional schemes for finite element discretizations on unstructured meshes has proved to be a particularly challenging task [20]. Furthermore, to our knowledge there is no published method for limiting the vector valued magnetic advection equation on a general unstructured grid.

The limiting procedure can be interpreted as reducing a high order numerical method to first order accuracy in the vicinity of a sharp discontinuity while maintaining the high order accuracy in the remaining regions where the solution is smooth. This requires a numerical procedure for detecting a shock (i.e. a "smoothness sensor") and a procedure for limiting (or reducing the order of) the advection update method by the proper amount to prevent spurious overshoots and undershoots. The theoretical foundations of this process were originally developed for 1D finite difference solutions to scalar conservation laws [35], [36], where the notion of a Total Variation Diminishing (TVD) method was introduced in order to guarantee a monotonic solution. As pointed out in [20], the generalization of the TVD criterion to finite element discretizations on 3D unstructured grids is the so called local extremum diminishing (LED) criterion [37]. The LED criterion is an algebraic statement which enforces the rule that local solution maxima cannot increase (thereby preventing spurious *overshoots*) and local minima cannot decrease (thereby preventing spurious *undershoots*). In this section, we follow the algebraic approach of [20] of modifying the discrete magnetic transport method so as to render the discretization local extremum diminishing.

Suppose we apply a limiting (or correction) term to the local face flux update equation (67) of the form

$$b_i^{lim} = b_i^{old} + \theta_i \Delta b_i$$

where the correction term θ_i has been introduced for each face flux. When $\theta_i = 1$, no limiting is performed and the flux update method is second order accurate. Now suppose we had a shock detector or smoothness sensor which could tell us whether or not the resulting face flux would result in a spurious overshoot or undershoot in the computation of $\vec{B}$. Our goal then is to compute the value of θ_i which would correct the flux update and prevent this from happening. However, we are immediately confronted with a problem. We cannot simply change the value of each face based flux independently, as this will clearly destroy the discrete divergence free property which we have worked so hard to obtain.

The key to overcoming this obstacle is to limit the edge based voltages rather than the face based fluxes. We therefore propose a divergence preserving limited update method of the form

$$\mathbf{b}^{lim} = \mathbf{b}^{old} - \mathbf{K}^{12}(\theta \mathbf{e}') \tag{74}$$

Since we are limiting (or correcting) independent edge based voltages, the update of (74) is guaranteed to be divergence preserving to machine precision. The general rule of thumb is that the edge based voltages which border the shock front are the ones responsible for the spurious overshoots / undershoots in the magnetic flux and must therefore be limited. However, in order to determine which edges are on the shock front and how much they need to be limited by, we need information from the face based fluxes, since we are ultimately concerned with obtaining a limited value of the discrete magnetic flux density $\vec{B}$ which is a face based quantity. An overview of this process is presented in Figure 5.

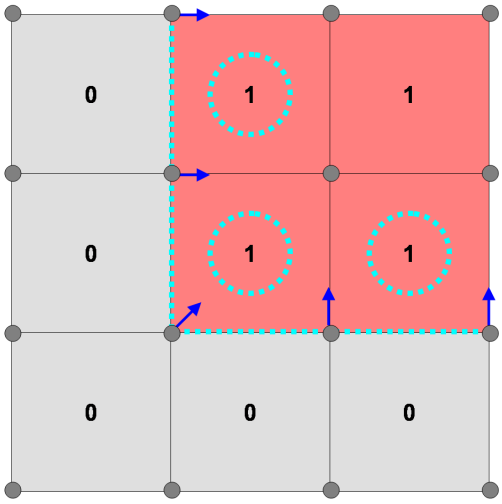

Fig. 5. Consider a patch of element faces in the presence of a discontinuous magnetic field oriented out of the page. In this example, the top four corner faces have unit magnetic flux while the remaining faces have no flux. If the nodes bordering the discontinuity were to move in the direction indicated, the unlimited flux update method would generate spurious overshoots in the three faces bordering the shock front (indicated with circles). These are the faces that require flux correction. To compute the divergence preserving flux correction, we limit the voltages on the edges which border the shock front.

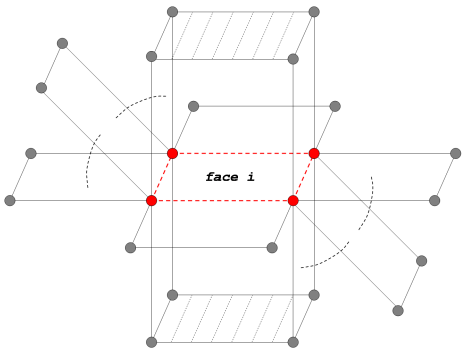

Fig. 6. Topological data structure used to detect discontinuities in face based fluxes. Note that the top and bottom faces are not used.

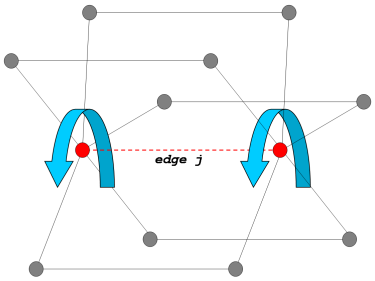

Fig. 7. Topological data structure used to detect discontinuities in edge based voltages.

The details of the process can be broken down into four steps:

- *Step 1* – Compute the unlimited flux change via (70)
- *Step 2* – Compute the face limited flux change via Algorithm 1
- *Step 3* – Loop over limited faces to determine the edges which lie along the shock front and compute the edge limiting factor via Algorithm 2
- *Step 4* – Compute the edge limited flux change by taking the limited curl via (74)

We begin by computing the unlimited flux change via the algebraic_constrained transport update of (70). Next, we compute a face limited flux change Δb by searching the topological data structure of Figure 6 using the method outlined in Algorithm 1. In other words, we check to see if the unlimited flux change will result in an overshoot or undershoot by searching all of the connected faces; if so, then we simply compute the limited value to be the maximum/minimum connected value of the data structure. The resulting limited flux change $\Delta\bar{b}$ could be used in the algebraic constrained transport update of (70) and it would result in a properly limited $\vec{B}$ field; however the resulting discrete $\vec{B}$ field would no longer be divergence free. Therefore, the next step is to determine which edges in the limited faces are responsible for the over/undershoots. In logical *u*-*v* (or reference) space, we can decompose a face into two sets of edges: the two edges parallel to the local *u* direction and the two edges parallel to the local *v* direction. Given a face that lies on the border of shock front, our goal is to compute which edge in each of these two sets requires limiting. This is accomplished by computing the "edge curl" using the topological data structure of Figure 7 according to the method outlined in Algorithm 2. Edges which border the shock front will have a large "edge curl" relative to the opposite edge in logical space. Once the limited edges have been identified, we calculate the edge limiting factor

$$\theta_j = \frac{\Delta b_i - \Delta\bar{b}_i}{\sum_{i=1}^{nlim} K_{i,j} e'_j} \tag{75}$$

Once this value has been computed for each limited edge, we can then compute the edge limited flux change via (74). Note that all of the information required for the data structures depicted in Figure 6 and Figure 7 is encoded in the topological derivative matrix $\mathbf{K}^{12}$ of (45), since this purely topological quantity is simply an incidence map which designates the connectivity between edges and faces.

6 Numerical Verification Experiments

In this section we present a series of numerical experiments which are designed to verify the individual components of our operator split discretization of MHD. For the first two examples of Section 6.1 and Section 6.2, we need to solve the linear system of (49) where the right hand side consists of an edge based finite element mass and stiffness matrix. For these examples we use a simple diagonally scaled pre-conditioned conjugate gradient (PCG) method which is sufficient for most applications. However we should point out that more advanced and efficient methods for solving linear systems arising from mixed finite element discretizations using $H(Curl)$ and $H(Div)$ basis functions exist, such as those employed in [25].

Algorithm 1: Face Based Shock Detection and Flux Correction

for $i = 1$ ***to*** *NumFaces* **do**
  //Compute the area of the old and new faces given their nodal coordinates
  A_i^{old} = `ComputeFaceArea(`*OldNodes*`);`
  A_i^{new} = `ComputeFaceArea(`*NewNodes*`);`
  $|B|^{old} = \frac{b_i}{A_i^{old}}$
  $|B|^{new} = \frac{b_i + \Delta b_i}{A_i^{new}}$
  //Initialize the max and min values
  $Max = Min = |B|^{old}$
  for $j = 1$ ***to*** *4* **do**
    for $k = 1$ ***to*** *NumConnectedFaces* **do**
      //Calculate local face extrema connected to edge j
      $A_{j,k}^{con}$ = `ComputeFaceArea(`*OldNodes*`);`
      $|B|^{con} = \frac{b_{j,k}}{A_{j,k}^{con}}$
      if $|B|^{con} > Max$ **then**
        $Max = |B|^{con}$
      else if $|B|^{con} < Min$ **then**
        $Min = |B|^{con}$
    end
  end
  //If face i is a local min or max, compute the limited value
  if $|B|^{new} > Max$ **then**
    $b_i^{lim} = Max * A_i^{new}$;
  else if $|B|^{new} < Min$ **then**
    $b_i^{lim} = Min * A_i^{new}$;
  $\bar{\Delta b_i} = b_i^{lim} - \Delta b_i$
end

6.1 Electromagnetic Diffusion in a Coaxial Cylinder at Rest

The purpose of this computational experiment is to verify the discrete electromagnetic diffusion operator L_σ of our operator splitting of the dynamo equation. Since we are ignoring the advection operator, we choose a simple test problem in which the conducting materials are at rest (i.e. $\vec{v}' = 0$). Furthermore, this test is designed to validate our approach for treating electromagnetic diffusion in highly heterogeneous conducting regions (i.e. regions consisting of conductors immersed in insulating vacuum like regions) using only a voltage source boundary condition. This test problem was developed in the spirit of the first test problem from [25]; however in this case we drive the problem with a voltage source boundary condition and we have an analytic solution to compare with.

In this computational experiment we apply a $1V$ potential difference across the ends

Algorithm 2: Edge Based Shock Detection and Voltage Correction

for $i = 1$ ***to*** *NumLimitedFaces* **do**
  for $j = 1$ ***to*** *4* **do**
    $\Delta e_j = 0$
    for $k = 1$ ***to*** *NumConnectedFaces* **do**
      //Compute the curl of $\vec{B}$ around edge j
      $A_{j,k}^{con}$ = `ComputeFaceArea(`*OldNodes*`);`
      $|B|^{con} = \frac{b_{j,k}}{A_{j,k}^{con}}$
      $\Delta e_j = \Delta e_j + K_{j,k} * |B|^{con}$
    end
  end
  //Check for shock in local u-direction
  Δe_u = `ComputeRatio(`$\Delta e_1, \Delta e_3$`);`
  //Check for shock in local v-direction
  Δe_v = `ComputeRatio(`$\Delta e_2, \Delta e_4$`);`
end

of a conducting coaxial cylinder and compute the steady state conduction current and magnetic field via the mixed FEM formulation of Section 3.3. The electrical resistance of the coaxial cylinder is given by

$$R = \frac{l}{\sigma A} \tag{76}$$

where l is the length of the coaxial cylinder and A is the cross sectional surface area of the coaxial cylinder determined by its inner radius R_i and outer radius R_o. The potential difference across the coaxial cylinder will result in a steady state conduction current density $\vec{J} = \sigma\vec{\nabla}\phi$ where ϕ is the scalar potential inside the conductor. We fix the geometry and conductivity σ of the problem such that the total resistance is $1\ \ Ohm$ and the total conduction current $I = 1\ \ Amp$. To facilitate the magnetic fields in the vacuum around the cylinder, the computational domain is a cylinder of radius $R_b = 2R_o$ and length l oriented along the $\hat{z}$ direction, divided into two material regions as shown in Figure 8. The cylinder is assigned a conductivity value $\sigma_c = 2S/m$ while the vacuum region is assigned a very small conductivity value $\sigma_{vac} = 10^{-7}\sigma_c$. The computational mesh consists of $5,760$ hexahedral elements.

The steady state magnetic field will have azimuthal symmetry which can be determined analytically from Ampere's law

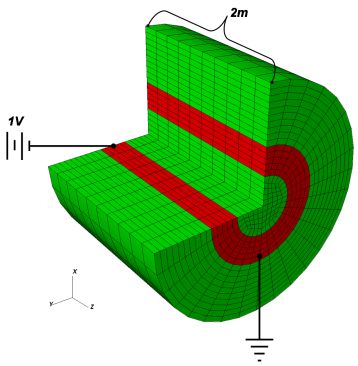

Fig. 8. Computational domain for conducting coaxial cylinder immersed in a vacuum like material.

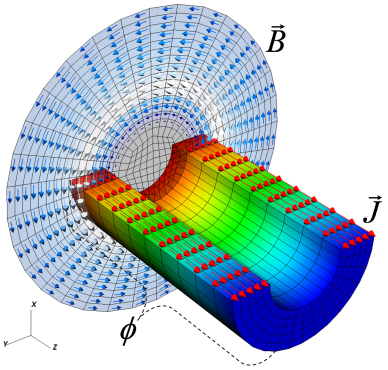

Fig. 9. Computed steady state electromagnetic fields for the conducting coaxial cylinder problem.

$$B_\theta(r) = \frac{\mu I_{enc}(r)}{2\pi r} \tag{77}$$

$$I_{enc}(r) = \begin{cases} 0 & r \le R_i \\ I\frac{r^2 - R_i^2}{R_o^2 - R_i^2} & R_i \le r < R_o \\ I & R_o < r \end{cases} \tag{78}$$

We can compute the total inductance in the computational region from an integral of the energy stored in the magnetic field via

$$L = \frac{\pi l}{\mu I^2} \int_0^{R_b} B_\theta^2(r) dr \tag{79}$$

Given the resistance R and the inductance L of the computational region, we can determine the exponential time dependence of the total current as it diffuses radially into the cylinder

$$I(t) = I\left(1 - \exp(-t\frac{R}{L})\right) \tag{80}$$

For the scalar potential solve of (48), we apply the inhomogeneous Dirichlet boundary condition $\phi = +1$ at the surface $z = 0$ and $\phi = 0$ at the surface $z = l$. For the discrete Ampere solve of (49), we apply the homogeneous Dirichlet boundary condition $\hat{n} \times \vec{E}^{ind} = 0$ over the entire surface of the problem domain. For both solves, a simple diagonally scaled PCG method with a residual error tolerance of 10^{-10} is used. We run the problem for a total time $t_{fin} = 3\tau$ where τ is one diffusion time constant such that $\tau = \sigma\mu(R_o - R_i)^2$, this will ensure that the fields reach steady state. We use a fixed time step $\Delta t = \frac{t_{fin}}{100}$. In Figure 9 we plot the scalar potential as well as the steady state conduction current density $\vec{J} = \sigma\vec{E}$ and magnetic field $\vec{B}$. In Figure 10 we plot the analytic solution for the azimuthal magnetic field as a function of radius and compare it with our mixed FEM solution. In Figure 11 we plot the total current as a function of time and compare it with our mixed FEM

solution.

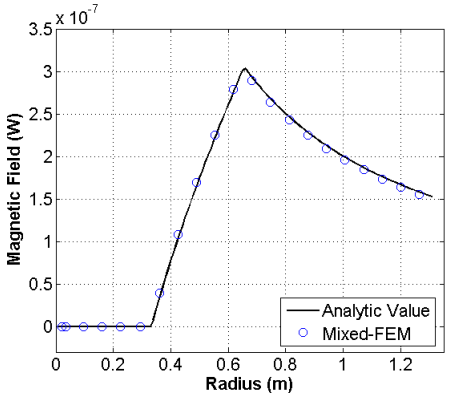

Fig. 10. Azimuthal magnetic field as a function of radius.

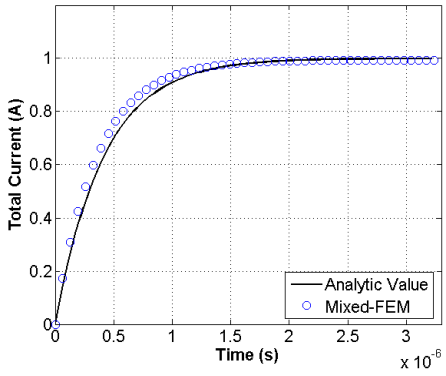

Fig. 11. Total current as a function of time

6.2 MHD Wave Propagation in an Ideal Gas

In this computational experiment we verify the coupling of the electromagnetic force to the equations of Lagrangian motion, which in turn will verify our Lagrangian treatment of the advection operator L_v. Our goal for this experiment is to launch waves and verify their computed velocity. A simple way to do this is to fix the velocity of the wave to some desired value, then to scale the domain size and total time for the problem such that the wave front just reaches the end of the computational domain at time $t = t_{fin}$. We consider the case of a rectangular "slab" mesh (i.e. one element thick in the z-direction) of dimension $2L_x$ by $2L_y$ centered at the origin $x = y = 0$ representing an ideal gas. We use a simple gamma-law model for the EOS of the gas given by

$$P = (\gamma - 1)\frac{\rho}{\rho_0}E \tag{81}$$

For an ideal monatomic gas, $\gamma = \frac{5}{3}$.

For reference, we first consider the case of a pure sound (or acoustic) wave. This is a purely hydrodynamic calculation and does not involve any electromagnetic properties. The sound speed is determined by the relation

$$v_s = \sqrt{\frac{\gamma P}{\rho}} \tag{82}$$

We choose a sound speed $v_s = 0.5m/s$ and an initial density $\rho = 1.0$. This determines the pressure which allows us to compute the energy for our EOS. We excite the wave by applying a time dependent velocity perturbation to a face in the mesh

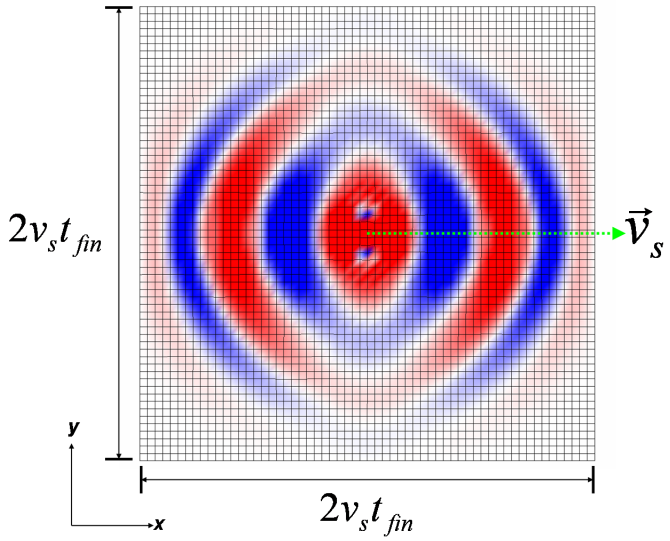

Fig. 12. Psuedocolor plot of velocity wave at time $t = t_{fin}$ for the case of a pure sound (or acoustic) wave. Since the initial velocity perturbation is oriented in the x-direction and the ideal gas has no strength, the velocity perturbation travels in the x-direction via compression waves at the sound speed v_s. The computational domain is a single element thick "slab" of dimension $2v_s t_{fin}$ by $2v_s t_{fin}$.

that is normal the x-axis and located at the center of the mesh. Specifically, we have

$$\vec{v}_{per} = A\cos(\omega t)\hat{x} \tag{83}$$

which gives us a displacement perturbation equal to

$$\vec{x}_{per} = \frac{A}{\omega}\sin(\omega t)\hat{x} \tag{84}$$

In order to keep the problem in the linear regime, we set the velocity perturbation amplitude to be $A = 10^{-2}$. For this experiment, the computational domain has dimensions $L_x = L_y = v_s t_{fin}$. We set the total time to be $t_{fin} = 1s$. This implies that the perturbation velocity (and displacement) will oscillate for two full periods during the simulation. Since the ideal gas has no strength (i.e. no restoring force orthogonal to the velocity perturbation), the velocity perturbation should propagate outward from the center of the mesh via compression and rarefaction waves traveling in the x-direction at the sound speed v_s as shown in Figure 12.

Now we consider the case of an MHD wave. We begin by applying an initial magnetic field to the problem domain oriented in the y-direction such that $\vec{B} = B_y\hat{y}$. For this case, we add an electrical conductivity to the ideal gas. We set the conductivity very high ($\sigma = 10^8 S/m$) so that the conducting gas effectively has no electrical resistance. This implies that our MHD diffusion equations are effectively loss-less for the time scales we are considering, meaning we are in the ideal MHD limit with the frozen in flux condition. We apply the same time dependent velocity perturbation

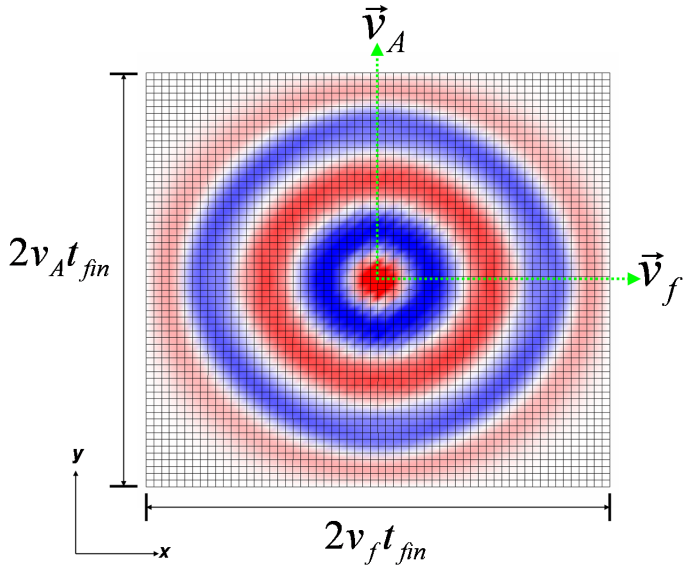

Fig. 13. Psuedocolor plot of velocity wave at time $t = t_{fin}$ for the case of an MHD wave, consisting of a fast (or magnetosonic) wave and a shear (or Alfven) wave. This is accomplished by adding a $\vec{B}$ field oriented in the y-direction to the problem. The velocity perturbation now travels in the x-direction via compression waves at the fast (or magnetosonic) speed v_f and in the y-direction via shear waves at the Alfven speed v_A. The computational domain is a single element thick rectangular "slab" of dimension $2v_f t_{fin}$ by $2v_A t_{fin}$.

in the x-direction to a face in the middle of the mesh. Because the magnetic field is "frozen in" to the material, it will be dragged along with the material as it moves. However, the $\vec{J} \times \vec{B}$ restoring force will work to resist this motion and effectively add strength to the gas in the from of the Maxwell stress tensor. We now expect to see two types of waves, a fast (or magnetosonic) compression wave traveling in the x direction at the speed v_f and a shear Alfven wave traveling in the y direction at the speed v_A as shown in Figure 13. The shear Alfven wave velocity is given by

$$v_A = \frac{|\vec{B}|}{\sqrt{\rho}} \tag{85}$$

while the fast (or magnetosonic) wave velocity is given by

$$v_f = \sqrt{v_s^2 + v_A^2} \tag{86}$$

We fix the Alfven speed to be $v_A = 1.0 m/s$ (which subsequently determines B_y) and keep the sound speed fixed at $v_s = 0.5 m/s$ as before; this implies the magnetosonic speed will be $v_f = \frac{\sqrt{5}}{2} m/s$. For the linear solve of (49) we apply the homogeneous Neumann boundary condition $\hat{n} \times \frac{1}{\mu}\vec{B} = 0$ to the x and y boundary planes (i.e. we are enforcing the constraint $\vec{v} \times \vec{B} = 0$ on the perimeter of the mesh). Since this is a three dimensional problem (i.e. it has finite depth in the z-direction), we apply the homogeneous Dirichlet boundary condition $\hat{n} \times \vec{E} = 0$ on the top and bottom of

the mesh defined by the planes $z = z_{min}$ and $z = z_{max}$. The linear solve is performed using a diagonally scaled PCG method with a residual error tolerance of 10^{-8}.

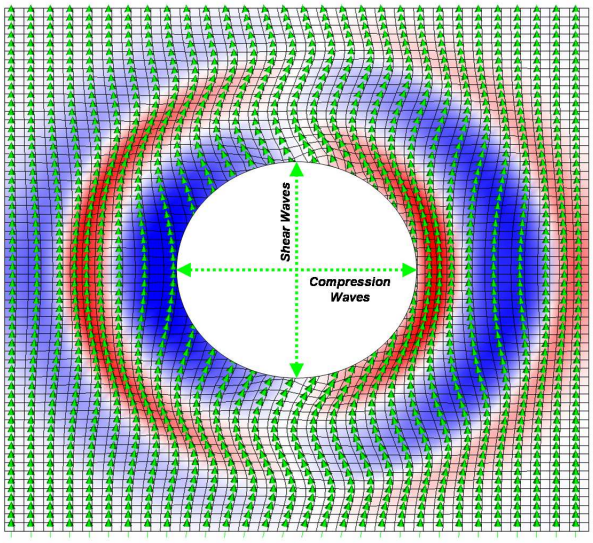

Fig. 14. MHD wave problem with exaggerated displacement (scale factor of 300) to emphasize the features of the Lagrangian calculation. Note how the mesh lines are parallel to the magnetic fields lines. The psuedocolor plot represents the magnitude of the magnetic field, $|\vec{B}|$. Here we can more clearly see the components of the Maxwell stress tensor in action. The pressure terms contribute to the peaks and nulls in the magnetic field magnitude along the *y*-direction due to compression waves while the deviatoric components give rise to the shearing motion of the vector field along the *x*-direction.

In Figure 14 we plot the magnetic field vectors and magnitude along with the computational mesh using an exaggerated displacement (scale factor of 300) to emphasize the characteristics of the Lagrangian calculation. Note how the mesh lines move with the magnetic field. In addition, note how the magnetic field lines compress and expand in the *y*-direction and undulate due to shearing motion in the *x*-direction. In Figure 15 we track the velocity wave amplitude to its first peak value for six different spatial locations along the Alfven wave axis (the *y*-axis). Note how the velocity wave amplitude decays at a rate proportional to $\frac{1}{\sqrt{r}}$, in direct agreement with the expected results for wave propagation in two dimensions (recall the Green's function for 2D wave propagation is proportional to $\frac{1}{\sqrt{r}}$). The peak to peak separation of the velocity wave amplitude at different points in time can be used to measure the instantaneous numerical velocity of the wave as shown in Figure 16. Note how the numerical Alfven wave travels at a non-constant rate which is slower than the expected constant rate, indicating the effects of numerical dispersion.

Finally, we perform the Lagrangian MHD wave calculation on a very unstructured mesh to test the robustness of the numerical method. In Figure 17 we compare the final results at time $t = t_{fin}$ for both mesh types, indicating that the proposed method can support MHD waves on highly unstructured grids with arbitrary connectivity.

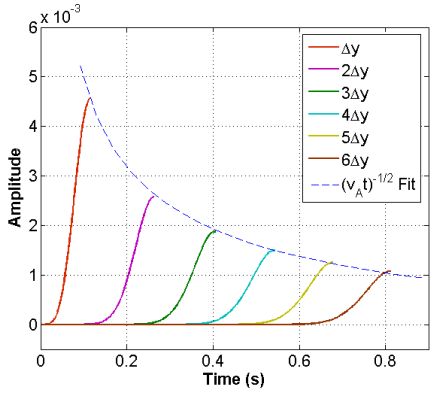

Fig. 15. Velocity wave amplitude as a function of time (up to first peak value) for six different spatial locations along the Alfven wave axis (y-direction) and a $\frac{1}{\sqrt{r}}$ fit to the amplitude.

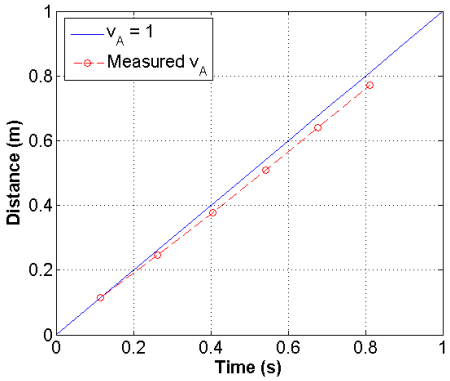

Fig. 16. Location of first peak value in velocity space for six different spatial locations, providing a measure of the instantaneous Alfven velocity as well as numerical dispersion.

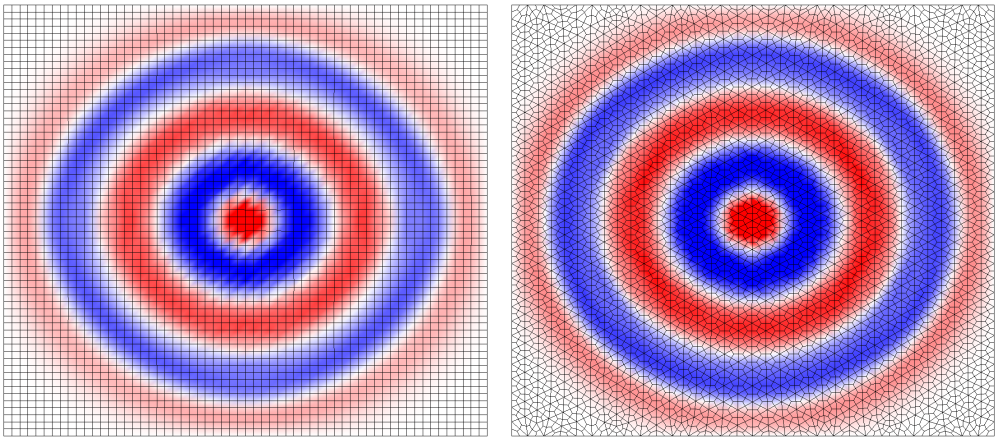

Fig. 17. Comparison of Lagrangian MHD wave results at time $t = t_{fin}$ for the case of a structured mesh (*left*) and a very unstructured mesh (*right*).

6.3 Eulerian Advection of Smooth Fields

The purpose of this computational experiment is to to demonstrate the second order accuracy of the algebraic constrained transport method of (70), and therefore verify our Eulerian treatment of the advection operator L_v. We consider the case of a "smooth" (i.e. infinitely differentiable) magnetic field initially projected onto a significantly distorted mesh. We then let the mesh relax to equilibrium while applying the constrained transport update of (70) at each mesh relaxation step to update the magnetic flux values. A sequence of images depicting this process is shown in Figure 18. We consider a solenoidal $\vec{B}$ field that can be expressed as the curl of a vector potential which represents a vector valued "Gaussian Hill" oriented in the $\hat{z}$ direction (i.e. out of the page)

$$\vec{A} = \exp\left(-\alpha(x^2+y^2)\right)\hat{z}$$
$$\vec{B} = \vec{\nabla} \times \vec{A}$$

The corresponding $\vec{B}$ field will have non-zero $\hat{x}$ and $\hat{y}$ components. We perform the calculation on a sequence of refined meshes and at each mesh relaxation step, the $L2$ finite element error is computed for each element, as shown in Figure 19. Note that the convergence of the method indicates second order accuracy.

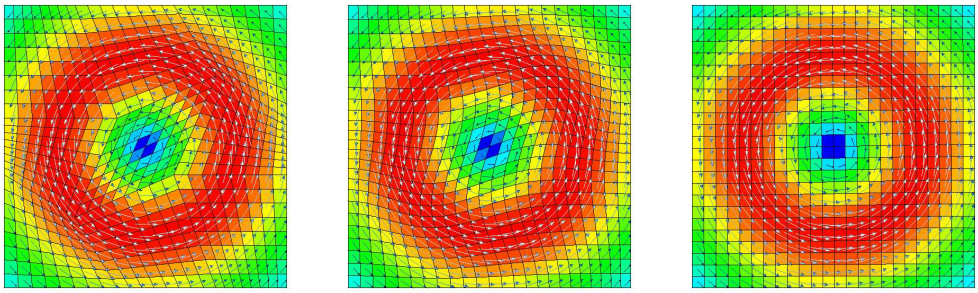

Fig. 18. A solenoidal magnetic field $\vec{B}$ is projected onto an initially distorted mesh (*left*). The mesh is then relaxed to equilibrium (*right*) via a sequence of steps (*middle*) while the magnetic flux is updated using the algebraic constrained transport method.

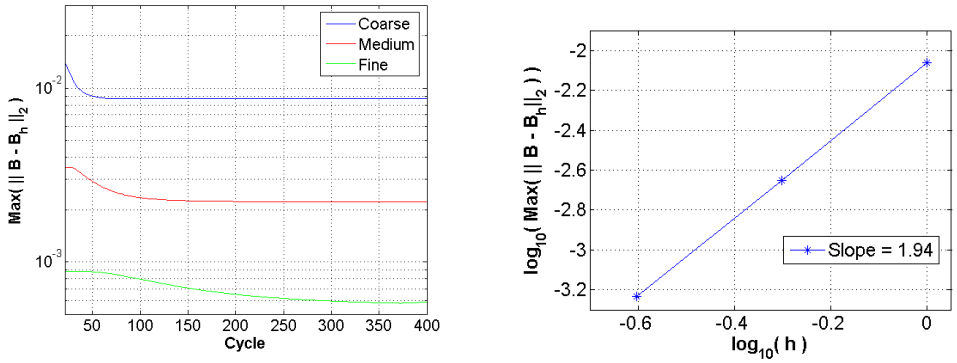

Fig. 19. Convergence analysis of finite element error for the magnetic advection equation using a coarse (144 element), medium (576 element) and fine (2,304 element) hexahedral mesh. The maximum $L2$ error vs. mesh relaxation cycle is plotted *left* while the maximum $L2$ error vs. element size at the final cycle is plotted *right* on a log scale, indicating the convergence rate is second order.

In addition, we compute the numerical energy stored in the magnetic fields at each mesh relaxation step as

$$\mathrm{e}_{mag} = \mathbf{b}^T \mathbf{M}^2(\mu^{-1})\mathbf{b} \tag{87}$$

In Figure 20 we plot the measured magnetic energy at each mesh relaxation cycle using three different limiting methods: no flux limiting (i.e. pure algebraic CT), face based flux limiting (i.e. non-divergence preserving) and edge based flux limiting (i.e. divergence preserving). Strict conservation of energy is not explicitly built into the method, and Figure 20 shows that some energy is lost during advection, even when no limiting is applied. The amount of lost energy is a function of the

mesh, and as the mesh is refined the amount of lost energy decreases with second order convergence. The fact that our advection method conserves magnetic flux exactly and conserves magnetic energy approximately is consistent with the hydrodynamics advection in ALE3D which conserves momentum exactly and conserves energy approximately. In Figure 21 we plot the total magnetic charge at each mesh relaxation cycle using the same three limiting methods. As expected, the unlimited and the edge limited algebraic CT method preserves the divergence of the $\vec{B}$-field to machine precision, independent of the mesh distortion. Note also how the face limited approach destroys the $\vec{\nabla} \cdot \vec{B} = 0$ property as expected.

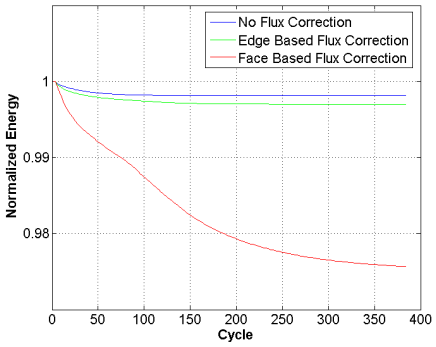

Fig. 20. Normalized magnetic energy at each mesh relaxation step using three different limiting methods.

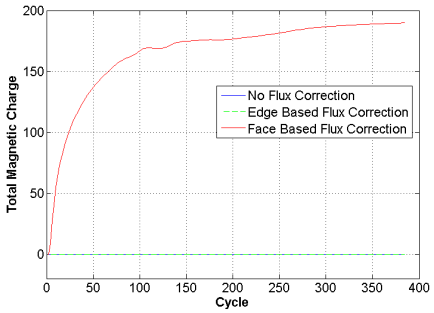

Fig. 21. Total magnetic charge at each mesh relaxation step using three different limiting methods.

6.4 Eulerian Advection of Discontinuous Fields

In these computational experiments we verify the algebraic flux correction method by performing mesh relaxation over discontinuous fields and verifying that the LED criterion is satisfied. We begin with a classic one dimensional advection problem adapted for our ALE treatment of magnetic flux. The computational domain and initial fields are depicted in Figure 22. We project onto the region two different initial vector fields. The first is a smooth Gaussian hill for reference purposes while the second is a unit step function. We apply an initial mesh density gradient to the computational domain such that one end has a high concentration mesh elements while the other end has a low concentration of mesh elements. When mesh relaxation is applied, the mesh will flow from the high density region to the low density region with the non uniform mesh velocity $\vec{v}_m$ until equilibrium is reached. This is equivalent to advecting the initial data in the opposite direction $-\vec{v}_m$. The results of this calculation with and without algebraic flux correction are shown in Figure 23. Note how spurious oscillations occurs at the leading and trailing edge of the shock front when no flux correction is applied. These results are in direct agreement with numerical advection of a square pulse using the textbook second order accurate Lax-Wendroff method. Note how the flux corrected result has succeeded in sup-

pressing the oscillations by directly enforcing the LED criterion. Furthermore, note that with and without flux correction, the results for the smooth function are are in good agreement with the initial data. This indicates that the proposed algebraic flux correction method does not introduce excess diffusion for smooth fields.

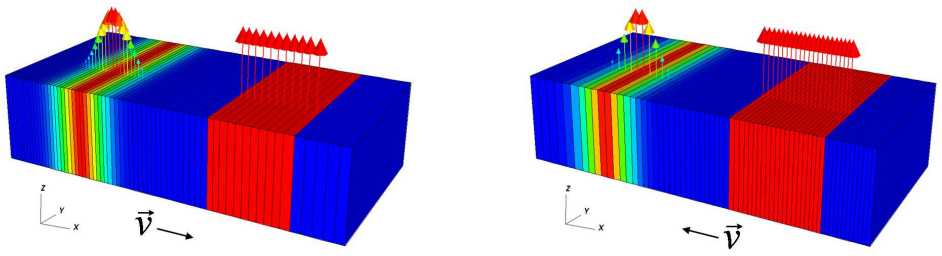

Fig. 22. Computational domain and initial field data for mesh relaxation over a smooth "Gaussian-hill" vector field and a discontinuous vector field. In both cases, the mesh is given an initial density gradient. When the mesh relaxation process is applied, the elements will flow from the region of high density to low density. In the first case (*left*) the mesh velocity will be from left to right while in the second case (*right*) the mesh velocity will be from right to left.

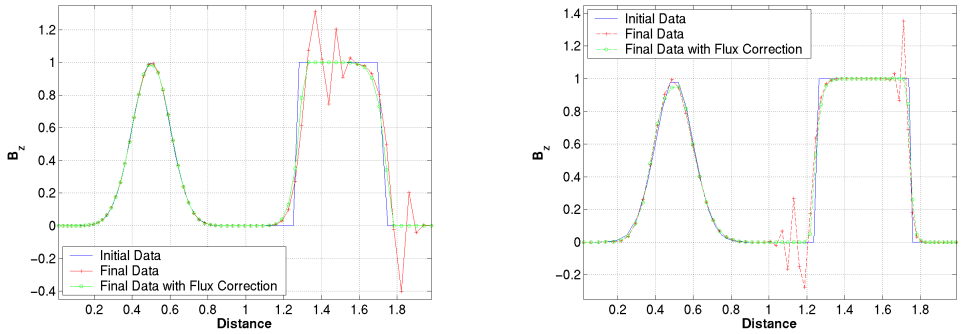

Fig. 23. Computational results for algebraic constrained transport of magnetic flux with and without algebraic flux correction for two different mesh velocity directions.

In Figure 24 we perform a similar experiment, except this time the computational domain is an unstructured cylinder mesh with a radial step function. Again, we apply an initial mesh density gradient to the computational domain. When mesh relaxation is applied, the mesh will flow radially inward / outward from high density region to the low density region with the non uniform mesh velocity $\vec{v}_m$ until equilibrium is reached. The results of this calculation with and without algebraic flux correction are shown in Figure 25. For the case of radial expansion, note how spurious undershoots in the magnetic flux density $\vec{B}$ occur at the shock boundary when no flux correction is applied while for the case of radial compression spurious overshoots occur. Note that in both cases, these spurious oscillations are suppressed when algebraic flux correction is applied.

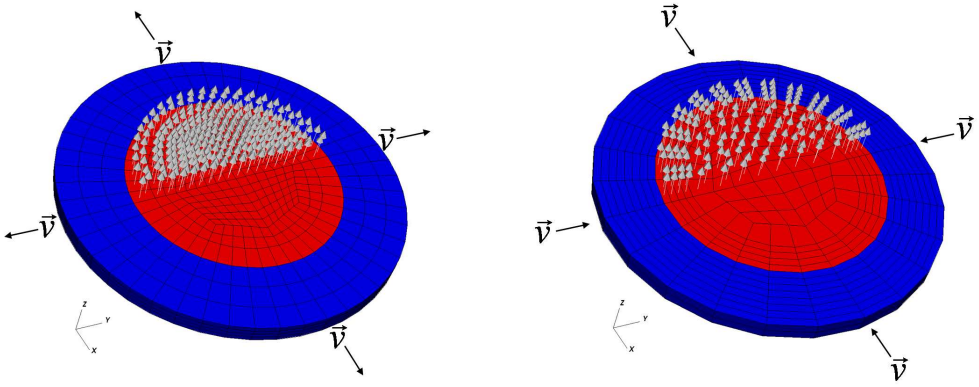

Fig. 24. Computational domain and initial field data for mesh relaxation over discontinuous vector field on an unstructured cylindrical mesh. In both cases, the mesh is given an initial density gradient. In the first case (*left*) the mesh will flow radially outward while in the second case (*right*) the mesh will flow radially inward.

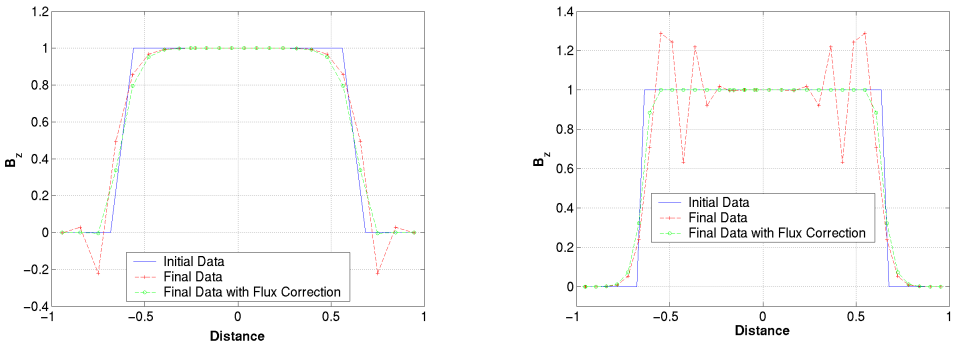

Fig. 25. Computational results for algebraic constrained transport of magnetic flux on an unstructured mesh with and without algebraic flux correction for two different mesh velocity directions.

6.5 Eulerian Treatment of MHD Wave Propagation

As mentioned previously, it is possible to implement a pure Eulerian formulation of MHD by computing a Lagrange step followed by a complete remap step in which the mesh snaps back to its original configuration at every time step. This is how ALE3D performs pure Eulerian calculations. In this section we revisit the MHD wave problem from Section 6.2 which was solved in a pure Lagrangian fashion (i.e. the computational mesh flowed with the conducting material). Here we perform the same calculation using a pure Eulerian process, meaning that at every time step, a Lagrange step is performed followed by an advective remap to the original unperturbed mesh. In Figure 26 we compare values for the amplitude of the magnetosonic wave at time $t = t_{fin}$ obtained in a pure Eulerian fashion against the original Lagrangian results of Section 6.2. Note how the two are in excellent agreement.

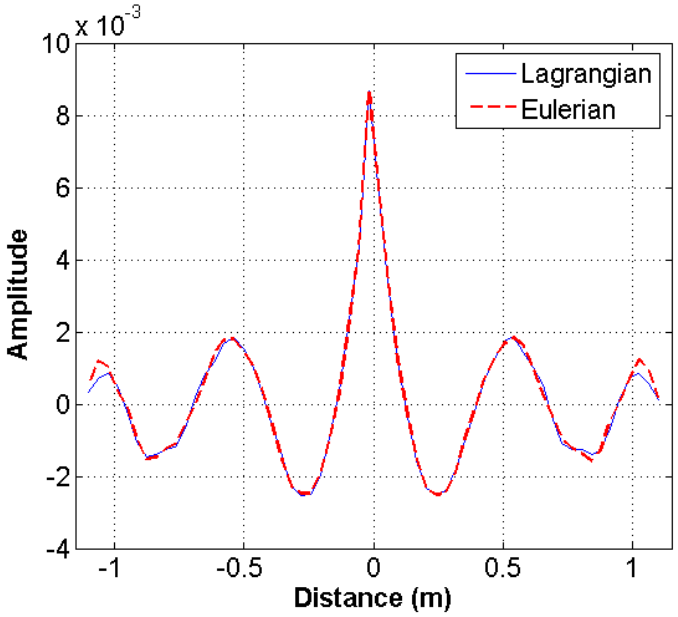

Fig. 26. Comparison of magnetosonic wave amplitude along the x-axis at time $t = t_{fin}$ for both Lagrangian and pure Eulerian calculations.

7 Conclusions

We have developed an arbitrary Lagrangian-Eulerian (ALE) discretization of resistive MHD on 3D unstructured grids. The method was formulated in an operator split manner with three distinct phases. We have argued that the operator splitting of the magnetic dynamo equation is particularly simple in the material (or Lagrangian) frame, and therefore a mixed finite element discretization using $H(Curl)$ and $H(Div)$ basis functions is naturally suited for such a problem. This is accomplished by constructing rectangular topological derivative matrices which represent the curl operator defined with respect to the material frame. We have employed the methodology of the finite element library FEMSTER to perform this discretization as it was designed specifically for these types of representations. Furthermore, we have developed a mixed finite element formulation of the dynamo equation that has a 2-form magnetic flux as its only state variable (making it amenable to advection), is second order accurate in time and supports explicit voltage source boundary conditions via an additional elliptic solve. For problems that require mesh relaxation and the subsequent remapping of state variables to the new mesh, via Eulerian advection, we have developed an algebraic constrained transport method which makes use of the rectangular topological derivative matrix. As such, the method is valid for 3D unstructured grids with arbitrary mesh velocity and is second order accurate for smooth magnetic fields. For discontinuous magnetic fields (e.g. MHD shocks), we have developed an algebraic flux correction method which limits an intermediate edge-based voltage in a manner that enforces a local extremum diminishing property on the magnetic flux. This algebraic flux correction is an intermediate step

in the algebraic constrained transport algorithm and hence $\vec{\nabla} \cdot \vec{B} = 0$ is still satisfied exactly. Finally, we have presented a series of numerical verification experiments which demonstrate the properties and accuracy of the proposed method.

References

[1] D. J. Benson. Computational methods in Lagrangian and Eulerian hydrocodes. *Comput. Methods Appl. Mech. Engrg.*, 99:235–394, 1992.

[2] T. Pierce and G. Rodrigue. A paralell two-sided contact algorithm in ALE3D. *Comp. Meth. Appl. MEch. Eng.*, 194(27):3127–3146, 2005.

[3] A. Nichols, R. Couch, J. Matlby, R. McCallen, I. Otero, and R. Sharp. Coupled thermal/chemcial/mechanical modeling of energetic materials in ALE3D. Technical Report UCRL-JC-124706, Lawrence Livermore National Laboratory, 1996.

[4] R. Couch, R. Sharp, I. Otero, R. Tipton, and R. McCallen. Application of ALE techniques to metal forming simulations. Technical Report UCRL-JC-114851, Lawrence Livermore National Laboratory, 1993.

[5] M. McClelland, J. Maienschein, A. Nichols, J. Wardell, A. Atwood, and P. Curran. ALE3D model predictions and materials charcterization for the cookoff response of pbxn-109. Technical Report UCRL-JC-145756, Lawrence Livermore National Laboratory, 2002.

[6] R. Couch and D. Faux. Simulation of underwater benchmark experiments with ALE3D. Technical Report UCRL-JC-123819, Lawrence Livermore National Laboratory, 1997.

[7] D. Stevens. Compressible multiphase flows in an ALE framework. Technical Report UCRL-JC-201373, Lawrence Livermore National Laboratory, 2003.

[8] C. Aro, E. Dube, and W. Futral. Coupled mechanical/heat transfer simulation on MPP platforms using a finite element linear solver interface. Technical Report UCRL-JC-131746, Lawrence Livermore National Laboratory, 1999.

[9] R. Tipton. A 2D lagrange MHD code. Technical Report UCRL-JC-94277, Lawrence Livermore National Laboratory.

[10] R. Tipton. Modeling flux compression generators with a 2D ALE code. Technical Report UCRL-JC-99900, Lawrence Livermore National Laboratory.

[11] G. Toth. The $\nabla \cdot B = 0$ constraint in shock-capturing magnetohydrodynamics codes. *J. Comput. Phys.*, 161(2):605–652, 2000.

[12] C. R. Evans and J. F. Hawley. Simulation of magnetohydrodynamic flows: A constrained transport method. *The Astrophysical Journal*, 332:659–677, 1988.

[13] J. M. Stone and M. L. Norman. ZEUS 2D - A radiation magnetohydrodynamics code for astrophysical flows in 2 space dimensions: II. The magnetohydrodynamic algorithms and tests. *Astrophysical Journal Supplement Series*, 80(2):791–818, 1992.

[14] D. S. Balsara and D. S. Spicer. A staggered mesh algorithm using high order Godunov fluxes to ensure solenoidal magnetic fields in magnetohydrodynamic simulations. *J. Comput. Phys.*, 149:270–292, 1999.

[15] D. S. Balsara. Second-order accurate schemes for magnetohydrodynamics with divergence-free reconstruction. *The Astrophysical Journal Supplement Series*, 151:149–184, 2004.

[16] D. S. Balsara and J. Kim. A comparison between divergence-cleaning and staggered mesh formulations for numerical magnetohydrodynamics. *The Astrophysical Journal*, 602:1079–1090, 2004.

[17] P. Londrillo and L. Del Zanna. High-order upwind schemes for multidimensional magnetohydrodynamics. *The Astrophysical Journal*, 530:508–524, 2000.

[18] J. M. Stone, J. F. Hawley, C. R. Evans, and M. L. Norman. A test suite for magnetohydrodynamic simulations. *Astrophysical Journal*, 388(2):415–437, 1992.

[19] R. E. Peterkin, M.H. Frese, and C.R. Sovinec. Transport of magnetic flux in an arbitrary coordinate ALE code. *J. Comput. Phys.*, 140(1):148–171, 1998.

[20] D. Kuzmin and S. Turek. High-resolution FEM-TVD schemes based on a fully multidimensional flux limiter. *J. Comput. Phys.*, 198(1):131–158, 2004.

[21] J. C. Nédélec. Mixed finite elements in R3. *Numer. Math.*, 35:315–341, 1980.

[22] R. Rieben and D. White. Verification of high-order mixed FEM solution of transient magnetic diffusion problems. *IEEE Trans. Mag.*, 42(1):25–39, 2006.

[23] J. D. Jackson. *Classical Electrodynamics*. 1962.

[24] M. Lax and D. F. Nelson. Maxwell equations in material form. *Phys. Rev. B*, 13(4):1777–1784, 1975.

[25] P. Bochev, J. Hu, A. Robinson, and R. Tuminaro. Towards robust Z-pinch simulations: Discretization and fast solvers for magnetic diffusion in heterogenous conductors. *Electronic Trans. Num. Analysis*, 15:186–210, 2003.

[26] A. Robinson. Personal communication, 2005.

[27] R. Rieben, D. White, and G. Rodrigue. A high order mixed vector finite element method for solving the time dependent Maxwell equations on unstructured grids. *J. Comput. Phys.*, 204:490–519, 2005.

[28] D. White, J Koning, and R. Rieben. *Compatible Spatial Discretizations*, volume 142 of *The IMA Volumes in Mathematics and its Applications*, chapter Development and Application of Compatible Discretizations of Maxwell's Equations. Springer-Verlag, 2006.

[29] P. Castillo, J. Koning, R. Rieben, and D. White. A discrete differential forms framework for computational electromagnetics. *Computer Modeling in Engineering & Sciences*, 5(4):331–346, 2004.

[30] R. Rieben, D. White, and G. Rodrigue. Improved conditioning of finite element matrices using new high order interpolatory bases. *IEEE Trans. Ant. Prop.*, 52(10):2675–2683, 2001.

[31] G. Rodrigue and D. White. A vector finite element time-domain method for solving maxwell's equations on unstructured hexahedral grids. *SIAM J. Sci. Comp.*, 23(3):683–706, 2001.

[32] P. Castillo, R. Rieben, and D. White. FEMSTER: An object orienetd class library of higher-order discrete differential forms. *ACM Trans. Math. Soft.*, 31(4):425–457, 2005.

[33] P. Bochev and M. Shaskov. Constrained interpolation (remap) of divergence-free fields. *Comput. Methods Appl. Mech. Engrg.*, 194:511–530, 2005.

[34] M. Berger and M. Aftosmis. Analysis of slope limiters on irregular grids. Technical Report 2005-0490, American Institute of Aeronautics and Astronautics.

[35] A. Harten. High resolution schemes for hyperbolic conservation laws. *J. Comput. Phys.*, 49:357–393, 1983.

[36] R. J. LeVeque. *Numerical Methods for Conservation Laws*. Birkhauser-Verlag, 1990.

[37] A. Jameson. Computational algorithms for aerodynamic analysis and design. *Appl. Numer. Math.*, 13:383–422, 1993.